Transportation Research Part C 174 (2025) 105086

Contents lists available at ScienceDirect

Transportation Research Part C

journal homepage: www.elsevier.com/locate/trc

Advancing lane formation and high-density simulations in bidirectional flow: A humanoid pedestrian model incorporating gait dynamics and body rotation

Xiaoyun Shang [a], Rui Jiang [a,*], S.C. Wong [b,*], Ziyou Gao [a], Wenguo Weng [c]

[a] School of Systems Science, Beijing Jiaotong University, Beijing 100044, PR China
[b] Department of Civil Engineering, The University of Hong Kong, Pokfulam Road, Hong Kong, PR China
[c] School of Safety Science, Tsinghua University, Beijing 100084, PR China

ARTICLE INFO

Keywords:
Humanoid pedestrian model
Body rotation
Lane formation
High-density bidirectional flow

ABSTRACT

Current bidirectional pedestrian flow models face challenges in accurately simulating lane formation and high-density conditions. This study addresses these issues by developing an improved humanoid pedestrian model (HPM), which extends the applicability of the original HPM from one-dimensional to two-dimensional scenarios and offers a more realistic simulation of pedestrian behavior. The improved HPM incorporates two distinct gaits—walking while rotating and walking while turning, which capture the complex dynamics of human walking—and an innovative gait-planning process. Additionally, a novel energy-based heuristic rule that considers factors such as deviation from the target direction, body rotation to navigate gaps, and reduced walking velocity is introduced. The energy expression is designed according to the form of mechanical energy, with no parameters requiring calibration. This design enables our model to demonstrate, to some extent, that pedestrians determine their walking direction by minimizing mechanical energy consumption. Simulations are conducted under conditions replicating previous experiments to validate the improved HPM against both experimental results and two classic models, namely the heuristic-based model and the social force model. The improved HPM shows minimal trajectory deviation; effectively replicates body rotation that facilitates efficient lane formation; and transitions swiftly from a randomized flow to stable, well-ordered flow patterns. Moreover, the improved HPM achieves a maximum density of 7 ped/m^2, representing a significant advancement in modeling high-density scenarios. Overall, the improved HPM offers deep insights into the crowd dynamics of bidirectional flow and thereby improves the accuracy of simulations in high-density situations.

1. Introduction

The movement of people through public spaces, particularly in high-density areas, has significant implications for both efficiency and safety. Thus, pedestrian flow studies are essential for urban planning and public safety. Over the past few decades, considerable efforts have been devoted to understanding pedestrian flow dynamics, with researchers concentrating on investigating pedestrian behavior from various perspectives. These studies have investigated the walking dynamics and standing balance of pedestrians

* Corresponding authors.
E-mail addresses: jiangrui@bjtu.edu.cn (R. Jiang), hhecwsc@hku.hk (S.C. Wong).

https://doi.org/10.1016/j.trc.2025.105086
Received 27 September 2024; Received in revised form 1 March 2025; Accepted 3 March 2025
Available online 14 March 2025

(Chatagnon et al., 2023, 2024; Jindrich and Qiao, 2009; Kubo et al., 2006; Smith and Lemaire, 2018; Snaterse et al., 2023), conducted experiments (Bacik et al., 2023; Feldmann and Adrian, 2023; Ma et al., 2021; Murakami et al., 2021; Nikolić et al., 2019; Seyfried et al., 2009), and developed models to simulate pedestrian flow (Helbing et al., 2005; Liang et al., 2021; Peng et al., 2024; von Sivers and Köster, 2015; Wageningen-Kessels et al., 2018; Zhai and Wu, 2020; Zhai et al., 2022) in various scenarios. These studies are not only crucial for urban planning and crowd management, but they also relate to other research fields such as humanoid robotics (Faraji and Ijspeert, 2017; Kajita et al., 2014), and crowd animations (Bruneau et al., 2015; Shoulson et al., 2014; Stüvel et al., 2017).

Bidirectional flow, a common pedestrian flow scenario, occurs at locations such as public transportation hubs, crosswalks, and event venues, and it is characterized by two groups of pedestrians moving in opposite directions. During bidirectional flow, a self-organization phenomenon known as lane formation often occurs, wherein pedestrians naturally align into distinct lanes to minimize conflict and enhance movement efficiency. The movement efficiency can be quantified by analyzing the flow–density relationship, commonly referred to as the fundamental diagram.

As pedestrian density increases, the probability of physical conflicts increases, which can lead to crowd turbulence and loss of control (Gu et al., 2025). Thus, high-density bidirectional flow is dangerous, particularly due to the risk of stampede incidents. For example, on December 31, 2014 in Shanghai, China, a stampede incident caused by clashes in a high-density counterflow on stairs resulted in 36 fatalities and 49 injuries (*https://edition.cnn.com/2015/01/21/world/china-shanghai-stampede*). This tragic event underscores the need to improve understanding of high-density bidirectional crowd characteristics to reduce the risk of stampede incidents.

Various experiments have been performed to investigate two main aspects of bidirectional flow, namely the lane formation process and the fundamental diagram, as described below.

Lane formation process: Two types of experiments have usually been performed to investigate the lane formation process. The first type of experiment is performed in a corridor with periodic boundaries, with all pedestrians randomly initialized. The second type of experiment is performed in a corridor with open boundaries, with two groups of pedestrians initially positioned at both ends of the corridor.

In the context of periodic-boundary conditions, Feliciani and Nishinari (2018) proposed a method for estimating congestion levels, allowing the detection of lane formation in a periodic bidirectional flow. Jin et al. (2019, 2021) conducted a series of experiments using corridors of varying widths and have observed five types of lane formation processes. They discussed various relationships, including those between lane formation results (such as types of lanes and formation times) and factors such as densities, corridor width, and the initial positions of pedestrians. Additionally, the influence of conditions such as umbrella holding (Guo et al., 2019) and limited visibility (Guo et al., 2016) on lane formation have been investigated. Spontaneous lane formation occurred when pedestrians held umbrellas, whereas pedestrian flow did not evolve into a stationary state under conditions of limited visibility.

In the context of open-boundary conditions, the identification of lanes has been investigated through various methods, i.e., cluster analysis (Hoogendoorn and Daamen, 2005), the Voronoi method (Zhang et al., 2012), and the order parameter method (Feliciani and Nishinari, 2016; Murakami et al., 2019, 2021). The order parameter method has been widely used to measure the stratification degree of bidirectional flow. For example, the onset of lane formation, as quantified by the order parameter, has been investigated through various experiments. It has been found that when two equal-sized groups walk toward each other in a 10 m $\times$ 3 m corridor without distraction, the onset of lane formation is approximately 4.5 s (Murakami et al., 2019, 2021). Moreover, experimental results indicated that, once lanes were formed, a balanced bidirectional flow was the most efficient, with a capacity comparable to that of unidirectional flow (Feliciani and Nishinari, 2016). In addition, it was found that the number of lanes is determined by pedestrian density and the initial distribution of pedestrians in the first row of a group (Zhang et al., 2022).

Several specific situations have been studied. These studies provide valuable insights into the dynamics of lane formation under various conditions. Murakami et al. (2021) demonstrated that mutual anticipation could contribute to self-organization through experiments involving distracted pedestrians. Furthermore, experiments with only two pedestrians walking toward each other revealed that spontaneous behavioral coordination during avoidance required mutual anticipation rather than mutual gaze (Murakami et al., 2022). Bacik et al. (2023) also showed that adherence to a "pass on the right" rule increased path lengths and passing times, suggesting that this rule should be used cautiously in crowd management.

Fundamental diagram: In general, walking velocity and flow rate decrease with increasing pedestrian density (Zhang et al., 2022), following a trend similar to that observed in unidirectional flow. However, Zhang et al. (2012) noted that bidirectional flow should not be interpreted as two unidirectional flows, as interactions between the opposing flows remain relevant, even though self-organized lanes can decrease head-on conflict.

Many experiments have been conducted to investigate the fundamental diagram in bidirectional flow (Feliciani and Nishinari, 2016; Guo et al., 2016; Zhang et al., 2011, 2012), and some have focused on high-density situations (Jin et al., 2019, 2021). Zhang et al. (2011, 2012) performed experiments using an open-boundary corridor, achieving a maximum local density of 4 ped/m^2. Jin et al. (2019, 2021) performed four large-scale pedestrian flow experiments in a periodic-boundary corridor, where all pedestrians were initialized randomly. In these experiments, a maximum local density of 11 ped/m^2 was obtained.

Furthermore, numerous models have been developed to study bidirectional flow phenomena, such as lane formation and the fundamental diagram. For instance, Yuan et al. (2017) extended the social force (SF) model (Helbing et al., 2000) by incorporating collision-avoidance forces and thereby successfully reproduced the lane formation phenomenon. Yi et al. (2023) improved the heuristic-based model (Moussaïd et al., 2011) by introducing heterogeneity and mutual anticipation. Under the same conditions in experiments (Murakami et al., 2021), this model predicted onset of lane formation at 6.36 s. Xiao et al. (2016) proposed a Voronoi diagram-based heuristics model, wherein a 5-m-wide corridor exhibited four to five lanes at a global density of 0.8 ped/m^2. Guo et al. (2016) improved the SF model by adjusting the driving forces and incorporating right-walking preferences, thereby achieving a

maximum local density of 3 ped/m^2 under the view-limited condition. The cellular automaton (CA) model (Blue and Adler, 2001) has also been developed through various methods. Bandini et al. (2014) presented specific extensions to the CA model, including overlapping and finer-grained extensions. They found that a cross-shaped pedestrian could move more flexibly than a square-shaped pedestrian and achieved a maximum density of approximately 6 ped/m^2 in an open-boundary corridor. Additionally, CA models have been devised that integrate body rotation behaviors (Fu et al., 2022; Jin et al., 2017; Miyagawa and Ichinose, 2020), where one pedestrian occupies two cells (0.2 m × 0.4 m), with two rotation angles (0° and 90°). This adaptation mitigated the deadlock in bidirectional flow, thereby achieving a maximum density of approximately 3 ped/m^2 in a periodic-boundary corridor (Jin et al., 2017) and 4.5 ped/m^2 in an open-boundary corridor (Fu et al., 2022). Recently, Fang et al. (2024) modified the CA model by adjusting body size, adding realistic velocity configurations, and extending lateral movement. The modified model successfully simulated bidirectional flow with density, thereby achieving 9 ped/m^2 in a periodic-boundary corridor. In addition, although lane occurrence probabilities closely matched the experimental results, the onset of lane formation significantly exceeded experimental observations.

Research gap: The above-mentioned studies have contributed to the understanding of bidirectional flow. However, current modeling research uses rather simple models, which do not adequately capture the detailed movements of pedestrians. Thus, there is a gap between empirical observations and theoretical models. A key limitation of current models is their limited capability to effectively simulate high-density scenarios. To the best of our knowledge, although continuum-space models (i.e., SF-based models and heuristic-based models) effectively reproduce lane formation, they fail to simulate high-density situations (>3 ped/m^2). This failure may be attributable to the neglect of body rotation. When the gap between two pedestrians is smaller than a pedestrian's body size, the passage of another pedestrian through the gap becomes impracticable even with body rotation, resulting in disorderly and chaotic flow, particularly under random initial conditions. Jin et al. (2017) introduced body rotation into the CA model, but the maximum density in a periodic-boundary corridor was 3 ped/m^2, which is low.

The improved CA model achieved a maximum density of approximately 6 ped/m^2 in an open-boundary corridor (Bandini et al., 2014), but its representation of cross-shaped pedestrians is unrealistic. Currently, an effective model for simulating high-density bidirectional flow is the CA model proposed by Fang et al. (2024), which achieved a maximum density of 9 ped/m^2 in periodic-boundary corridor. However, compared with experimental observations, the model requires a much longer time to establish stable flow from initially random distributions. Moreover, the model does not address the conflict between pedestrians moving longitudinally and those moving laterally. Furthermore, CA-based models are limited in their ability to accurately reproduce the lane formation process. This limitation is due to their inability to enable precise adjustments in walking direction and speed for lane formation. That is, pedestrians controlled by CA-based models can only make discrete jumps between adjacent cells, which hinders their capacity to make subtle, small-scale adjustments in walking direction.

To overcome the key limitations of the previously described models, the humanoid pedestrian model (HPM), which integrates body rotation and stepping behavior (Shang et al., 2024), was developed. The HPM has demonstrated strong performance in one-dimensional (1D) scenarios, including single-file movement and bi-directional flow in narrow corridors (Shang et al., 2024). In the narrow-corridor scenario, collisions are avoided as pedestrians rotate their bodies, which represents one of the strategies introduced in the enhanced HPM. In this improved model, pedestrians navigating a 2D plane can avoid conflicts by either adjusting their walking direction or rotating their bodies. The effects of body rotation on stepping behavior are seamlessly incorporated into the 3D skeletal framework.

This advancement resolves challenges encountered by the SF model and heuristic-based models in simulating dense bidirectional flows. Thus, in periodic-boundary corridors, the maximum density in the HPM increased to 7 ped/m^2, with body sizes of approximately 0.25 m × 0.45 m. Additionally, the lane formation process in HPM simulations aligned better with experimental results in both periodic- and open-boundary corridors than that in previously developed model simulations. Specifically, the time required for lane formation was significantly reduced compared with that required by the model proposed by Fang et al. (2024) and thus closely resembled experimental observations.

The rest of this paper is organized as follows. Section 2 presents the improved HPM. Section 3 introduces three datasets and the simulation setups. Section 4 provides the simulation results. Section 5 is the conclusion.

Table 1
Definitions of gait parameters for ped_i.

Gait parameter	Definition
$\boldsymbol{T}_i^n$	Start moment of the n th step
Δ_i^n	Step duration of the n th step
$\boldsymbol{P}_i(t)$	Set of all joint positions at time t
$\boldsymbol{X}_i(t); \boldsymbol{X}_i^n$	Gait parameter at time t; gait parameter of the n th step
$\boldsymbol{l}_i(t); \boldsymbol{l}_i^n$	Step length at time t; step length of the n th step
$\boldsymbol{w}_i(t); \boldsymbol{w}_i^n$	Step width at time t; step width of the n th step
$\boldsymbol{\theta}_i(t); \boldsymbol{\theta}_i^n$	Shoulder orientation at time t; shoulder orientation of the n th step
ω_i	Sway angle
γ_i^n	Target direction of the n th step
$\boldsymbol{F}_i^{sw}; \boldsymbol{F}_i^{st}$	Swing foot; support foot
$\boldsymbol{G}_i^n$	Walking gait of the n th step

2. HPM

The original HPM described in Shang et al. (2024) represents a pedestrian as a multi-link system with 11 degrees of freedom (DoFs). This model performs well in 1D situations, where pedestrians walk along a predetermined route with a fixed direction.

In this paper, the HPM is extended to higher-dimensional situations to form an improved HPM. Both the walking direction and the body rotation angle are determined using an energy-based heuristic rule. Subsequently, some crucial gait parameters are calculated. Moreover, a novel gait is introduced to depict walking behaviors that involve temporary directional changes, such as collision avoidance. This new gait enables pedestrians to adjust their walking direction by modifying their step width and step length.

The general definition of the state of a pedestrian *ped* in this paper is as follows:

$$ped = \langle P, X, \Delta, G \in \{G_R, G_T\}\rangle \tag{1}$$

where $P \in \mathbb{R}^{3\times|J|}$; $|J|$ is the number of joints; $P^j(t) \in \mathbb{R}^{3\times1}$ is the position of the j th joint at time t; $X = [l, w, \theta, \gamma, \omega]^T$ is a set of gait parameters, defined in Table 1 and in Section 2.1.2; Δ is the step duration; and G denotes the current gait. For instance, G_R indicates walking while rotating, and G_T indicates walking while turning. Each gait has three states that indicate walking difficulty, i.e., N,D,E, which represent "normal," "difficult," and "easy" walking, respectively.

As proposed in Shang et al. (2024), a step consists of a double-support phase and a single-support phase. The double-support phase is simplified as a standing moment, making the step duration Δ equal to the single-support phase duration. The definitions of the temporal parameters are given in Table 1, whereas the temporal structure of the HPM is shown in Fig. 1.

Fig. 2a depicts the HPM framework. Upon completing the n th step, the positions of all joints $P(T_n)$ are calculated and then the support foot is switched. The gait-design process involves several key stages: identifying pedestrians at risk of collision; determining the avoidance direction and body rotation angle; selecting an appropriate gait; and calculating a collision-free step length and step width. During the single-support phase, the swing foot steps forward based on the predefined rules, and the positions of all joints are updated at each time step. Furthermore, a collision avoidance mechanism is integrated into the simulation.

2.1. Body modeling

A pedestrian in the HPM is modeled as a 3D skeleton with 11 DoFs (see Fig. 2(b)). The method of calculating body joint positions and the lengths of links ($L_1 - L_8$) are detailed in our previous work (Shang et al., 2024). The support foot is aligned with $\boldsymbol{n}(\gamma)$, where $\boldsymbol{n}(\cdot) = (\cos(\cdot), \sin(\cdot), 0)$.

2.1.1. Definitions of the two gaits and the gait parameters

The definitions of avoidance direction α and five gait parameters X, namely step length (l), step width (w), shoulder orientation (θ), and target direction (γ), lateral sway angle (ω) (Kuo, 1999), are illustrated in Fig. 3. The velocity is always aligned with the avoidance direction, as defined below:

$$\vec{v(\alpha)} = \frac{\sqrt{l^2 + \left(w - L^p\right)^2}}{\Delta}\vec{n(\alpha)} \tag{2}$$

where L^p denotes the pelvis width, which is equal to L_3 in Fig. 2(b), and Δ denotes the step duration for the current step, and it corresponds to the step length and width, as discussed in Section 2.2.3.

The angle of orientation corresponding to the target direction γ is denoted as θ, which equals $\frac{\pi}{2}$ when walking without rotating, whereas the body rotation angle equals $\frac{\pi}{2} - \theta$.

Moreover, the equivalent mapping between the three rotation angles and five physical variables is as follows: $\{l, w, \theta, \gamma, \omega\} \overset{\mathscr{B}}{\rightarrow} \{\theta_{1\text{-}4}, \psi_{1\text{-}3}, \varphi_{1\text{-}4}\}$. A gait corresponding to a gait parameter X is marked as $\mathscr{B}(X)$, as detailed in Section 2.3.1 and in Shang et al. (2024).

Before introducing different gaits, the distinction between avoidance direction α and target direction γ is first clarified. As shown in Fig. 2(b), γ represents the direction of the support foot in the absolute coordinate system and is also the target direction. In contrast, α is the actual walking direction, which may temporarily deviate from γ to allow a pedestrian to avoid collisions with other pedestrians. In

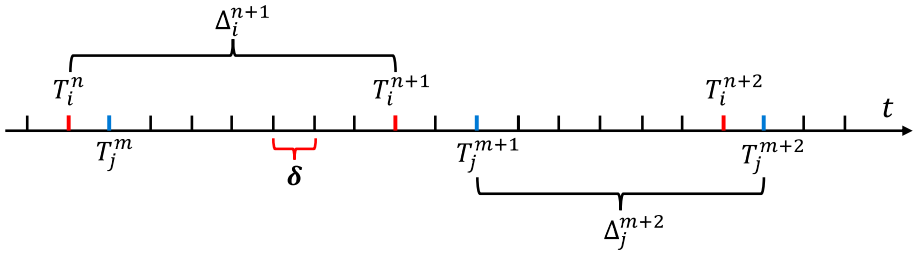

Fig. 1. Temporal structure of the HPM, where δ is the time step, and i and j denote two different pedestrians.

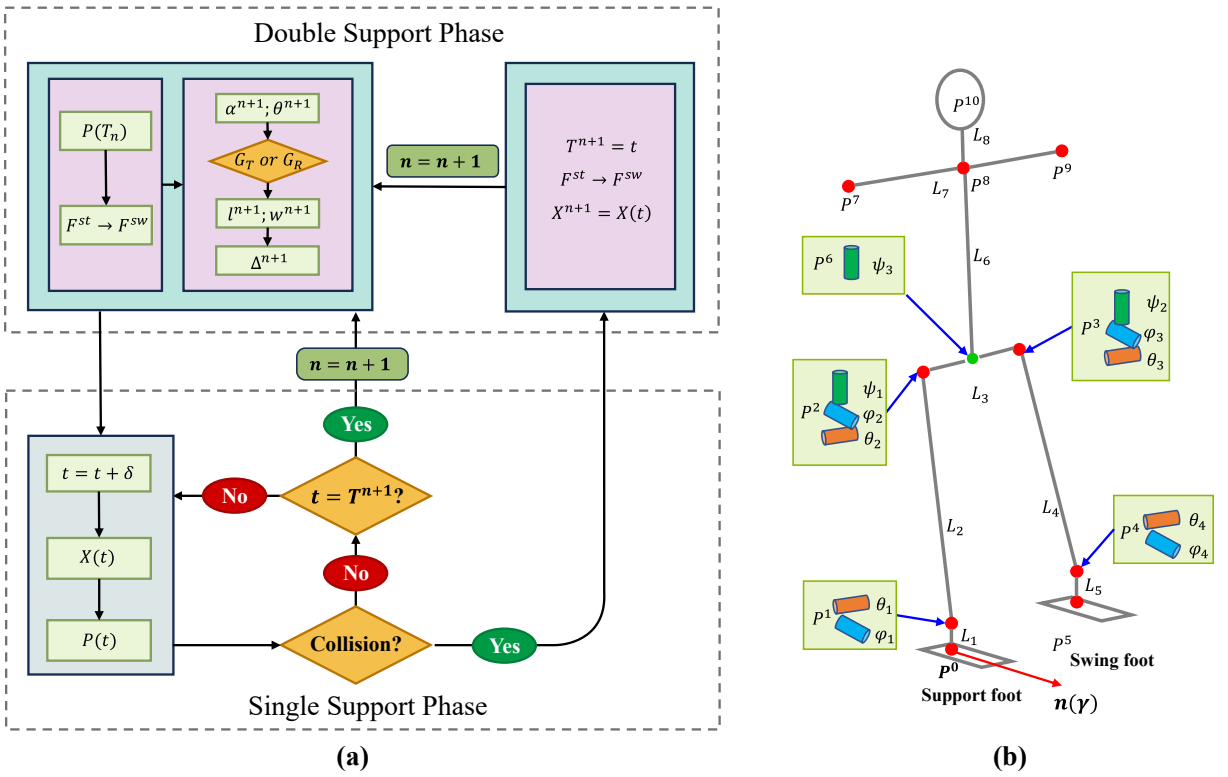

Fig. 2. (a) Schematic of the HPM framework. The gait parameters are calculated during the double support phase. (b) Schematic of a 3D skeleton with 11 DoFs. The three orthogonal rotation angles ψ, θ, φ are known as Euler angles. The red arrow on the support foot indicates the target direction γ; a detailed explanation is provided in Section 2.1.1.

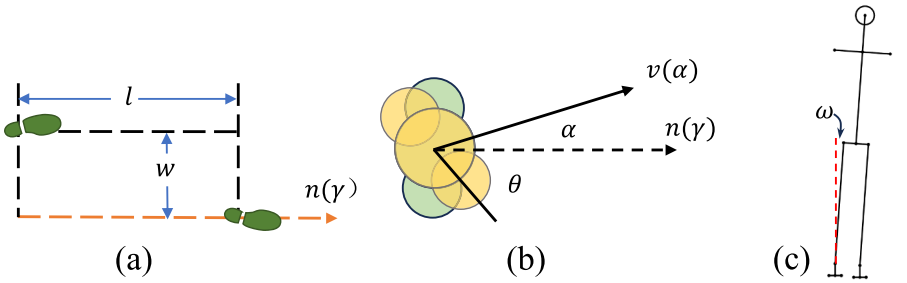

Fig. 3. (a) Definitions of l and w, where $n(\gamma)$ is represented by the orange dashed arrow and is the target direction. (b) Definitions of θ and α, where the green figure indicates the torso without rotation, that is $\theta = \pi/2$. (c) Definition of ω. Note: (a) and (b) are from a superior viewpoint, whereas (c) is from an anterior viewpoint.

the original HPM, pedestrians walk along a predetermined route with a fixed direction. Hence, there is no difference between α and γ, i.e., they are aligned with the route, such as a circular track. However, in the improved HPM developed in this paper, pedestrians walk on a 2D plane and continually adjust their directions to avoid collisions. Thus, α and γ are different and not aligned with the route.

This paper focuses primarily on bidirectional flow as the first step in developing the HPM for 2D scenarios. In bidirectional flow, pedestrians walk along a straight corridor with a fixed target direction, and the target direction γ remains constant, aligned with the corridor.

The following part of this section discusses different walking gaits and their effects. Walking consists of the three fundamental behaviors described below.

Walking while rotating (G_R): Pedestrians apply this type of gait so that they can rotate their body to pass through a narrow corridor or avoid pedestrians walking in the opposite direction when the lateral distance between them is small. This type of gait is depicted in Fig. 4(a).

Walking while turning (G_T): Pedestrians apply this type of gait when changing their walking direction or avoiding conflicts. It is

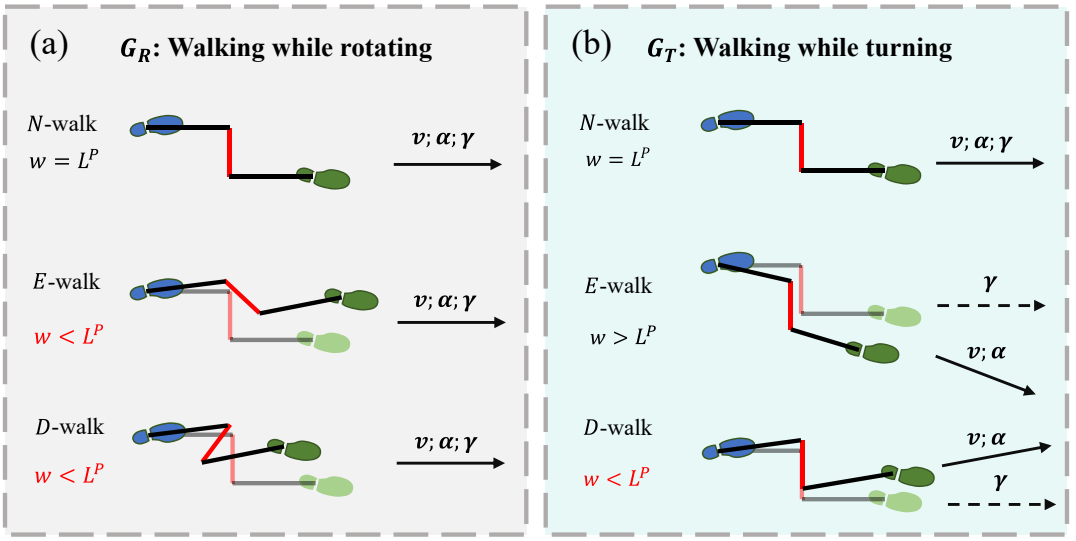

Fig. 4. Two walking gaits, namely (a) G_R: walking while rotating; and (b) G_T: walking while turning. Both subfigures are from a superior viewpoint. The foot in blue (green) represents the support (swing) foot; the black line represents the leg; and the red line represents the pelvis, which is perpendicular to the target direction. In the second and the third rows, the light-colored lines and shapes indicate the *N*-walk state. In addition, $\boldsymbol{\alpha}$ and $\boldsymbol{\gamma}$ represent $\boldsymbol{n}(\alpha)$ and $\boldsymbol{n}(\gamma)$, respectively.

applied using one of three strategies, as shown in Fig. 5: lateral foot placement, such as sidestepping; external rotation of the foot, resulting in a change in γ; and a combination of the aforementioned two strategies.

Normal walking: Normal walking can be considered as a state of gait G_R or G_T, such as walking with no rotation (the *N*-walk of gait G_R) or walking in a straight-line without turning (the *N*-walk of gait G_T), as shown in the first row of Fig. 4.

When pedestrians walk in bidirectional flows in a straight corridor, their directional changes are typically temporary, i.e., performed to avoid conflicts, which can be achieved through simple sidestepping (Fig. 5(a)). In contrast, in scenarios such as exit-directed evacuations, directional changes are more longer lasting and may involve more complex turning behaviors, such as adopting more energy-efficient turning strategies. Therefore, this paper makes some simplifications. First, only the lateral foot placement strategy for gait G_T is adopted, as shown in Fig. 4(b). Second, body rotation behavior is employed during only straight-line walking, where the avoidance direction α aligns with the target direction γ, as shown in Fig. 4(a).

The three states of gait G_R were thoroughly discussed by Shang et al. (2024). In summary, body rotation intrinsically impacts stepping behavior. Gait states *D* and *E* describe the relationship between the rotation direction and the support foot. For example, when a pedestrian rotates in a counterclockwise direction, it is easy (difficult) for the pedestrian to step forward with the right (left) foot. This state is denoted as the *E*-walk (*D*-walk) of gait G_R. In contrast, walking without rotation is denoted the *N*-walk of gait G_R, as shown in Fig. 4(a).

Similar states are defined for gait G_T. Thus, gait states *D* and *E* describe the relationship between the turning direction and the support foot. For example, left turning is more easily achieved by stepping laterally with the left foot rather than with the right foot, as the latter requires stepping to the left side of the body while avoiding conflict with the support foot. The state in which the turning direction and the support foot are the opposite (the same) is denoted as the *E*- (*D*-) walk of gait G_T. In contrast, walking without turning is the *N*-walk of gait G_T, as shown in Fig. 4(b). These three states of gait G_T are consistently observed in experimental trajectories during collision avoidance tasks, as illustrated in Fig. 6.

In the HPM, it is assumed that the swing foot is not permitted to collide with the support foot in gait G_T. Thus, the permissible stepping boundary for the *D*-walk of gait G_T is determined by the relative positions of the two legs, which correspond to the boundary

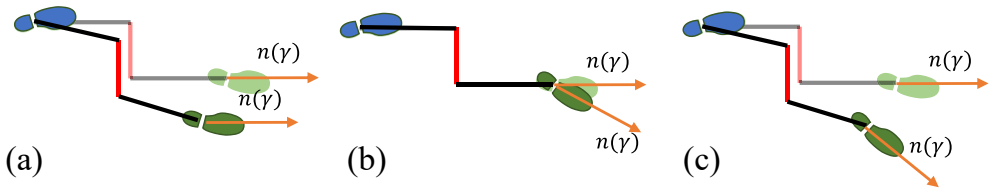

Fig. 5. Three strategies for walking while turning: (a) lateral foot placement; (b) external rotation of orientation γ, i.e., rotation of the foot toward a desired direction; (c) a combination of the strategies in (a) and (b). All three subfigures are from a superior viewpoint, and the light-colored lines and shapes indicate the *N*-walk state. The foot in blue (green) represents the support (swing) foot; and the red and black lines indicate the pelvis and leg, respectively.

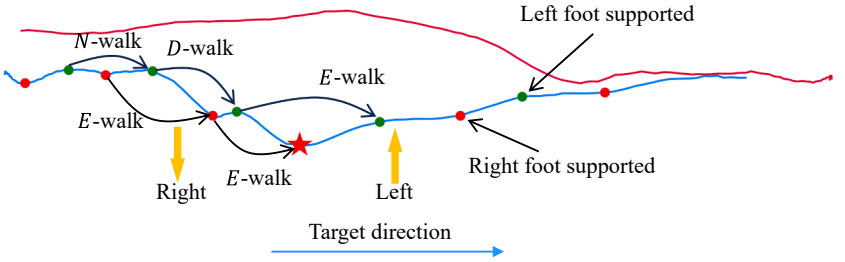

Fig. 6. The 22nd pair of experimental trajectories provided by Murakami et al. (2022). The body sways during the transition of the support foot. As a result, the support foot can be inferred from the trajectory. For example, the red and green dots indicate the positions of the right and left support foot, respectively, of a pedestrian on the blue trajectory (Ding et al., 2024). This pedestrian begins on the left side and moves to the right to avoid another pedestrian walking in the opposite direction on the red trajectory. Specifically, before the red star, the pedestrian on the blue trajectory makes a right turn in three steps, transitioning from an *E*-walk to a *D*-walk, and then to an *E*-walk. The distinction between these two walking states is clearly illustrated by the relative positions of the successive support-foot placements.

of the yellow area in Fig. 7. Additionally, the stepping boundary for the *E*-walk of gait G_T is represented by the boundary of the blue area. The step radius $R = \sqrt{l^2 + (w - L^p)^2}$ ranges from 0 to the free-walking step length l^F. Once R and the avoidance direction α are determined, the step length l and step width w can be obtained from the intersection point of the avoidance direction and the stepping boundary.

As the avoidance direction α and target direction γ are aligned for gait G_R, the calculation of step length and width is basically the same as that in Shang et al. (2024). However, instead of shoulder width, as used by Shang et al. (2024), this paper uses body orientation θ to determine the step width for gait G_R. The step radius R in Fig. 7 is equivalent to the step length l and its maximum value R^{max} is depicted in Table A1.

Therefore, the step length and width can be obtained from the avoidance direction α, the step radius R, and the body orientation θ. The determination of these parameters is detailed in Section 2.2. The joint rotation angle values corresponding to the gait parameters for gaits G_R and G_T are given in Appendix A.

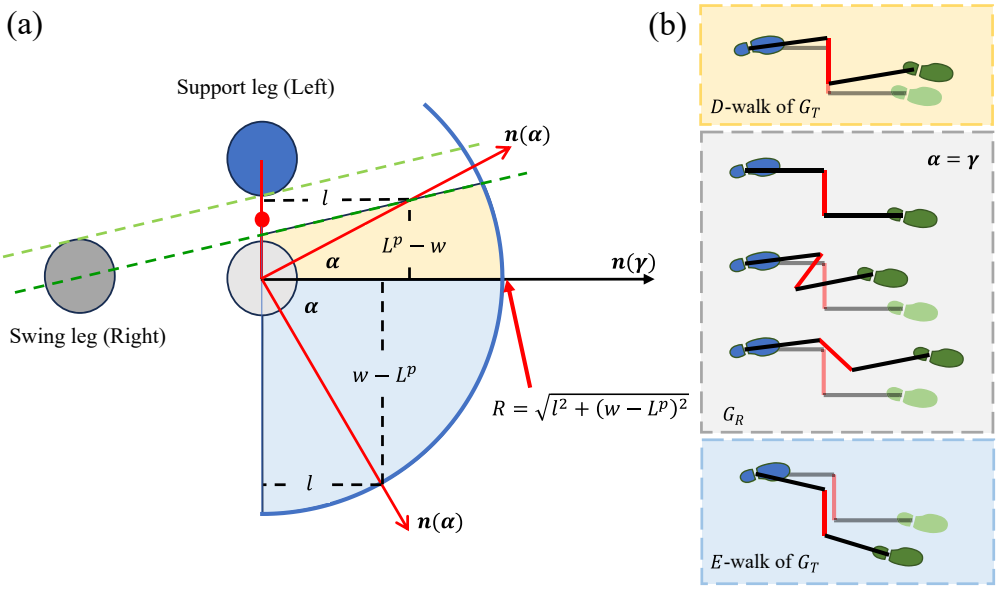

Fig. 7. Overview of the relationship between avoidance direction α, step radius R, the relative positions of the legs, and two walking gaits. In (a), the pedestrian moves to the right, with the positions of the legs indicated by blue and gray circles, respectively. The radius R_l corresponds to the thigh radius of an adult. When the pedestrian is standing on the support leg (blue circle), the position of the swing leg is indicated by a light-gray circle. The distance between the centers of the blue and light-gray circles equals L^p. A blue dashed semicircle with radius R is centered at the light-gray circle. The light-green dashed line is tangential to both the blue and gray circles. The swing leg moves along the green dashed line to avoid conflicting with the support leg. Thus, the boundary of the yellow area in (a) represents the collision-free range of the swing foot when turning left while standing on the left foot. This walking state corresponds to the *D*-walk of G_T in (b). Similarly, the boundary of the blue area in (a) represents the stepping range of the swing foot when turning right while standing on the left foot, corresponding to the *E*-walk of G_T in (b). If $\alpha = \gamma$, the gait is G_R, as depicted in (b).

2.2. Double-support phase

This section introduces a novel method for planning a pedestrian's gait during the double-support phase. This method is inspired by the principle of least effort (PLE), a general theory first proposed in 1949 by Zipf, who observed that "*an organism will expend the least average rate of work, as estimated by itself*" (Zipf, 1949). Additionally, "*The basic idea is that living beings naturally choose the path to their goal that they expect will require the least amount of 'effort'*" (Guy et al., 2010). PLE has been observed in human walking behavior, which occurs in a manner that minimizes metabolic energy (Donelan et al., 2001). Furthermore, PLE has been widely applied in simulations to create energy-efficient trajectories (Guy et al., 2010) and footsteps (Singh et al., 2011).

According to this concept, we propose a new energy-based heuristic rule to determine the optimal avoidance direction and the corresponding body orientation. The gait for the next step is then selected from the available gaits, G_R and G_T. The step radius is defined as the longest collision-free distance in the avoidance direction. Additionally, the step length and width are calculated using the method illustrated in Fig. 7. The step duration is determined by the step length and width.

2.2.1. Energy-based heuristic rule

This section focuses solely on the shoulder motion of pedestrians, as body rotation is a shoulder-dominated movement and there has been limited research on walking behavior in 2D situations (Ma et al., 2021). Simplifying the human body into an elliptical or three-circled shape is a common approach in pedestrian flow simulations (Chraibi et al., 2010; Farina et al., 2017; Peng et al., 2024; Song et al., 2019; Xu et al., 2019; Yamamoto et al., 2019). In this section, a pedestrian is modeled as a three-circled shape for the calculation of gait parameters, as illustrated in Fig. 8.

For ped_i, the set of pedestrians at risk of collision, denoted as obs_i, can be defined as the n pedestrians walking in the opposite direction and closest to ped_i within ped_i's vision field within a radius D_i^v, which ranges from $\gamma_i - \frac{\pi}{2}$ to $\gamma_i + \frac{\pi}{2}$.

The collision-free body orientation in direction $\alpha \in \left[\gamma_i - \frac{\pi}{2}, \gamma_i + \frac{\pi}{2}\right]$, $\theta_i(\alpha)$, is defined as follows:

$$\theta_i(\alpha) = \min_{j \in obs_i; w \in Wall} \left(\theta_i^j(\alpha), \theta_i^w(\alpha)\right) \tag{3}$$

where, $\theta_i^j(\alpha)(\theta_i^w(\alpha))$ represents the maximum body orientation $\theta \in \left[0, \frac{\pi}{2}\right]$ that ped_i can adopt while walking in direction α without colliding with ped_j (where w is the wall index).

The infeasible directions comprise directions in which collision occurs after a 90° rotation ($\theta_i(\alpha) = 0$), and directions in which collision occurs within one step.

The cost of a step in feasible direction α is defined as the energy spent in executing a foot-stepping action. The avoidance direction α_i^{n+1} for the $n+1$ th step is obtained by minimizing the cost. Three forms of energy are modeled for a step: E_1, which is the cost of deviation from the target direction; E_2, which is the cost of rotating the body to pass through a narrow gap; and E_3, which is the cost of walking at a slow velocity. Thus, the total cost of a step in a given direction is given by

$$E(\alpha) = E_1 + E_2 + E_3 \tag{4}$$

Therefore, the cost of deviation from the target direction γ is modeled as follows:

$$E_1(\alpha) = M\Delta\alpha = J_1\omega_p\omega_e\Delta\alpha = \left(J_{C1} + m_i L_i^{l2}\right)\frac{||v_i^n||}{L^l}\frac{\Delta\alpha}{T^0}\Delta\alpha \tag{5}$$

where J_1 and J_{C1} are the moments of inertia about the ankle and the center of mass rotating in the sagittal plane, respectively; m_i is the body mass of ped_i; L_i^l is the leg length, which is L_2 (L_4) in Fig. 2(b); $\Delta\alpha = |\alpha - \gamma|$ is the deviation from the target direction; $||v_i^n||$ is the velocity of ped_i at the n th step; and T^0 is the minimum step duration.

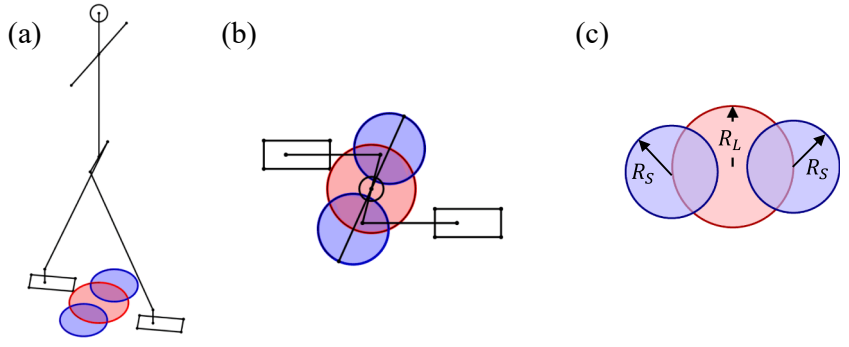

Fig. 8. Schematic of a pedestrian from (a) a lateral viewpoint and (b) a superior viewpoint, where the three circles represent the torso. (c) Details of the three circles; the body depth equals $2R_L$, and the shoulder width (L_7 in Fig. 2(b)) equals $2R_L + 2R_S$.

Furthermore, the cost of body rotation is given by

$$E_2(\alpha) = \frac{1}{2}J_2\omega^2 = \frac{1}{2}\left(J_{C2} + m_i\left(\frac{L_i^P}{2}\right)^2\right)\left(\frac{\Delta\psi}{T^0}\right)^2 \tag{6}$$

where J_2 and J_{C2} are the moments of inertia about the support foot and the center of mass rotating in the transverse plane, respectively; and $\Delta\psi = \frac{\pi}{2} - \theta_i(\alpha)$ is the body rotation angle.

When ped_i walks in the target direction without body rotation, the sum of E_1 and E_2 is 0. This scenario includes a specific situation in which another pedestrian is walking very close to ped_i in the same direction and on the same target path as ped_i, with no other pedestrians walking in alternate directions, i.e., along the red arrow in Fig. 9(a). $E_1 + E_2$ equals 0 in this scenario, prompting ped_i to choose to walk slowly in the target direction rather than moving into unused space. This ultimately leads to irregular high-density lanes forming in the bidirectional flow.

To address this issue, the cost of walking at a slow velocity, E_3, is introduced and defined as follows:

$$E_3(\alpha) = \frac{1}{2}m_i\left(v_i^{0\,2} - \left(\frac{d(\alpha)}{kT^0}\right)^2\right) \tag{7}$$

where v_i^0 is ped_i's free-walking velocity; $d(\alpha)$ is the maximum distance that ped_i can walk in direction α without colliding with other pedestrians after time kT^0; and k is a random number in the interval of [1, 2]. $d(\alpha) = kv_i^0T^0$ when no pedestrian occupies direction α within the range of $kv_i^0T^0$, as indicated by the black arrow in Fig. 9(c). $d(\alpha) = 0$ when there is a potential collision in direction α, as indicated by the red dashed arrow in Fig. 9(c).

The optimal avoidance direction for the $n+1$ th step is obtained by minimization of the modified cost function $E(\alpha)$:

$$\alpha_i^{n+1} = \mathit{argmin}(\mathscr{F}(\alpha)E(\alpha)) \tag{8}$$

where $\mathscr{F}(\alpha) = \mathscr{F}_1(\alpha) + \mathscr{F}_2(\alpha)$ is a penalty function consisting of two components, as detailed below.

Punishment for the *D*-walk of gait G_T: When turning right and turning left are equivalate in the cost function, i.e., $E(\gamma + \Delta\alpha) = E(\gamma - \Delta\alpha)$, pedestrians tend to choose a turning direction that is opposite to the support foot, i.e., they turn left with the right foot as the support foot. Thus, the corresponding punishment is defined as follows:

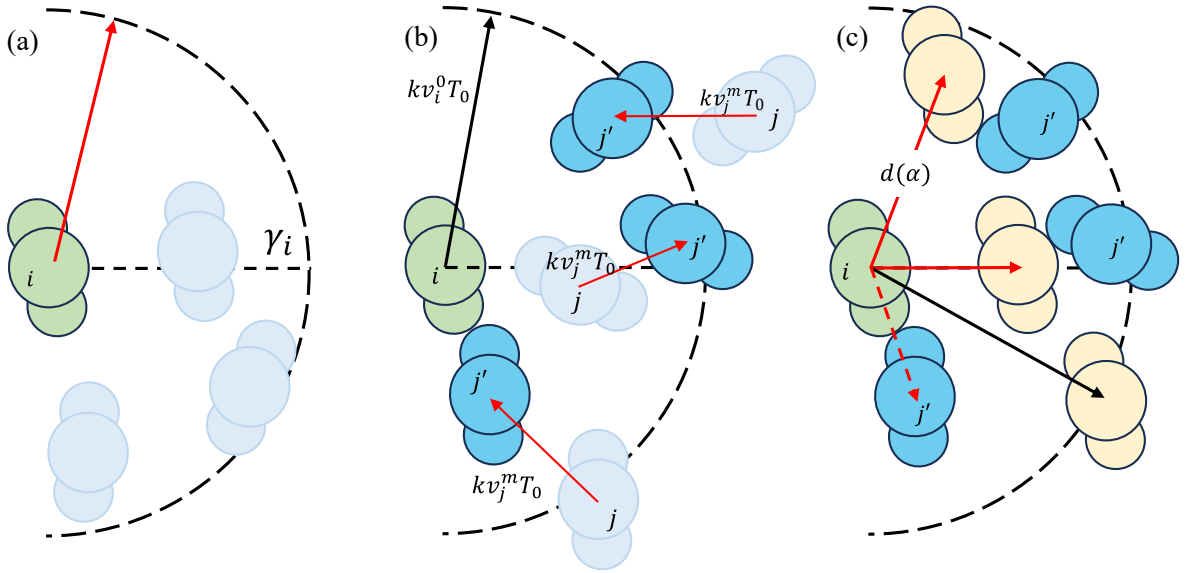

Fig. 9. Schematic for calculating E_3. In (a) and (b), ped_i and other pedestrians at current time ($t = T_i^n$) are represented by the green and light-blue three-circled shapes, respectively. In (a), if ped_i does not slowly walk behind the pedestrian in front but walks along the path indicated by the red arrow, ped_i can walk faster in an unused space. (b) The calculation of E_3 considers the pedestrians who are very close to ped_i after time kT^0 and are represented by blue three-circled shapes. v_j^m is ped_j's previous velocity ($t \in \left(T_j^m, T_j^{m+1}\right)$). (c) The length of a solid arrow indicates the magnitude of $d(\alpha)$. The dashed red arrow indicates a potential collision after time kT^0. In this case, $d(\alpha)$ is set to 0.

$$\mathscr{T}_1(\alpha)=\begin{cases}1+\left(\dfrac{2\kappa_1|\alpha-\gamma_i|}{\pi}\right)^2, & \left(F_i^{st}=R \text{ and } g(\gamma_i,\alpha)<0\right) \text{ or } \left(F_i^{st}=L \text{ and } g(\gamma_i,\alpha)>0\right)\\ 1, & otherwise\end{cases} \tag{9}$$

where $g(\gamma_i,\alpha)$ indicates the turning direction, which is the third term of $\boldsymbol{n}(\gamma_i)\times\boldsymbol{n}(\alpha)$; $g(\gamma_i,\alpha)$ equals 1 when turning left and −1 when turning right; and κ_1 is a constant.

Punishment for frequently changing turning direction: When turning right and turning left are equivalate in the cost function, pedestrians tend to use the turning direction they used in the former step. The corresponding penalty function is defined as follows:

$$\mathscr{T}_2(\alpha)=\begin{cases}1+\left(\dfrac{2\kappa_1|\alpha-\gamma_i|}{\pi}\right)^2, & g(\gamma_i,\alpha)^{*}g\left(\gamma_i,\alpha_i^n\right)<0\\ 1, & otherwise\end{cases} \tag{10}$$

Moreover, the body orientation for the $n+1$ th step of ped_i, θ_i^{n+1}, is $\kappa_2\theta_i\left(\alpha_i^{n+1}\right)$, where κ_2 is a constant that ensures a safe distance is maintained between two pedestrians and between ped_i and walls.

2.2.2. Gait selection

As mentioned in Section 2.1.1, the avoidance direction α and target direction γ are aligned for gait G_R. Therefore, when α_i^{n+1} is close to γ_i, the gait of G_R is selected as follows:

$$G_i^{n+1}=\begin{cases}G_R, & \left|\alpha_i^{n+1}-\gamma_i\right|\le\kappa_3 \text{ and } \theta_i^{n+1}<\dfrac{\pi}{2}\\ G_T, & otherwise\end{cases} \tag{11}$$

where κ_3 is a constant. Once the gait of G_R is selected, the avoidance direction α_i^{n+1} is set to γ_i, and the rotation direction is dependent on the current step, thereby ensuring that the first step is always an E-walk.

The maximum distance that ped_i can walk in direction α_i^{n+1} with body orientation θ_i^{n+1} is denoted as d_i^{n+1}. Thus, the step radius in Fig. 7 is defined as follows: $R_i^{n+1}=\min(\kappa_2 d_i^{n+1}, l_i^F)$. l_i^F represents the free walking step length. Its value can be found in Table A1 for gait G_R and Table A3 for gait G_T.

2.2.3. Step duration

The method used for calculating step duration in this paper is essentially the same as that used in our previous work (Shang et al., 2024), but with certain simplifications.

The step duration is determined by using an inverse proportional function $\mathscr{T}$ and a randomness ε_{lw} to measure the change degree in the step length and width, as follows:

$$\Delta_i^{n+1}=\max\left(T^0,\mathscr{T}+\epsilon_1\beta_1\varepsilon_{lw}\right) \tag{12}$$

$$T\left(R_i^{n+1}\right)=\min\left(T^{upp},\max\left(T_0,\frac{\beta_2}{R_i^{n+1}}\right)\right) \tag{13}$$

$$\varepsilon_{lw}=\frac{\left|R_i^{n+1}-R_i^n\right|}{l_i^F} \tag{14}$$

where β_1 is a constant; ϵ_1 is a uniform random number in the interval of [-1, 1]; and $\mathscr{T}(\cdot)$ is an inverse proportional function, which has the step radius, a constant of proportionality β_2, a lower bound T^0, and an upper bound T^{upp} as arguments.

2.3. Single-support phase

This section describes the changing rules for the gait parameter in the single-support phase and details a mechanism for collision avoidance.

2.3.1. Changing rules for the gait parameters

The position of the support foot in the single-support phase ($t\in\left(T_i^n,T_i^{n+1}\right]$) is the position of the swing foot at the end of the n th step, $P_i^5\left(T_i^n\right)$. All the joint positions, $P_i(t)$, are determined by both the gait parameter at time t, $X_i(t)$, and $P_i^5\left(T_i^n\right)$. Thus, $P_i(t)$ is obtained from the corresponding gait $\mathscr{B}(X_i(t))$ shifting (represented by "$\oplus$") to $P_i^5\left(T_i^n\right)$, as follows:

$$P_i(t)=\mathscr{B}(X_i(t))\oplus P_i^5\left(T_i^n\right),\ t\in\left(T_i^n,T_i^{n+1}\right] \tag{15}$$

During the single-support phase, the variation of the gait parameter is modeled as shown in Eqs. (16). Specifically, the change in

step length is considered to be an acceleration process followed by a deceleration process (Chung et al., 2012; Huang et al., 2018), as described in Eq. (16d). Furthermore, the step width, body orientation, and sway angle are assumed to change uniformly, and ω_0 is a constant. The target direction γ is set to remain unchanged.

$$X_i(t) = X_i\left(\tau + T_i^n\right) = QX_i\left(T_i^n\right) + \int_0^\tau A(t)dt \tag{16a}$$

$$Q = diag\{-1, 1, 1, 1, 1\} \tag{16b}$$

$$A(t) = \left[A_l(t), \frac{w_i^{n+1} - w_i^n}{\Delta_i^{n+1}}, \frac{\theta_i^{n+1} - \theta_i^n}{\Delta_i^{n+1}}, 0, A_\omega(t)\right]^T \tag{16c}$$

$$A_l(t) = \begin{cases} \dfrac{l_i^{n+1} + l_i^n}{\left(\frac{1}{2}\Delta_i^{n+1}\right)^2} t, \ t \in \left(0, \dfrac{1}{2}\Delta_i^{n+1}\right] \\ \dfrac{l_i^{n+1} + l_i^n}{\left(\frac{1}{2}\Delta_i^{n+1}\right)^2} \left(\Delta_i^{n+1} - t\right), \ t \in \left(\dfrac{1}{2}\Delta_i^{n+1}, \Delta_i^{n+1}\right] \end{cases} \tag{16d}$$

$$A_\omega(t) = \begin{cases} 2\omega_0 \dfrac{t}{\Delta_i^{n+1}}, \ t \in \left(0, \dfrac{1}{2}\Delta_i^{n+1}\right] \\ 2\omega_0 \left(1 - \dfrac{t}{\Delta_i^{n+1}}\right), \ t \in \left(\dfrac{1}{2}\Delta_i^{n+1}, \Delta_i^{n+1}\right] \end{cases} \tag{16e}$$

2.3.2. Collision avoidance

The stepping movement of ped_i spans multiple model updates. During this period, if other pedestrians do not maintain the consistent walking speeds expected by ped_i, a collision may occur. To determine whether a pedestrian has collisions during the single-support phase, the collision boundaries are estimated using five circles, i.e., three circles on the torso and two circles on the feet. These five-circle boundaries are employed to detect potential collisions with nearby pedestrians, as shown in Fig. 10. If any of ped_i's five circles contacts any of the other pedestrians' circles, ped_i prematurely ends the current step, and thus $X_i^{n+1} = X_i(t)$.

3. Data sources

3.1. Overview of referenced datasets

In this section, three datasets provided by Jin et al. (2021) and Murakami et al. (2021, 2022) are reviewed and compared with the simulation results across the following three aspects.

Individual trajectories: One of the most fundamental interactions in pedestrian dynamics is the avoidance behavior between two pedestrians. In a series of experiments conducted by Murakami et al. (2022), two pedestrians walked toward each other in opposite directions along a corridor. One pedestrian was asked to exhibit one of three conditions: to do nothing in particular (the "BASE" condition), to perform a typing task on a mobile phone while walking, or to wear mirrored sunglasses. Each condition was replicated 120 times. For the analysis in the current paper, only the 120 pairs of trajectories from the BASE condition are utilized and are denoted as *TrajE*.

Lane formation process: The model is tested in a collective context, specifically focusing on the lane formation process in

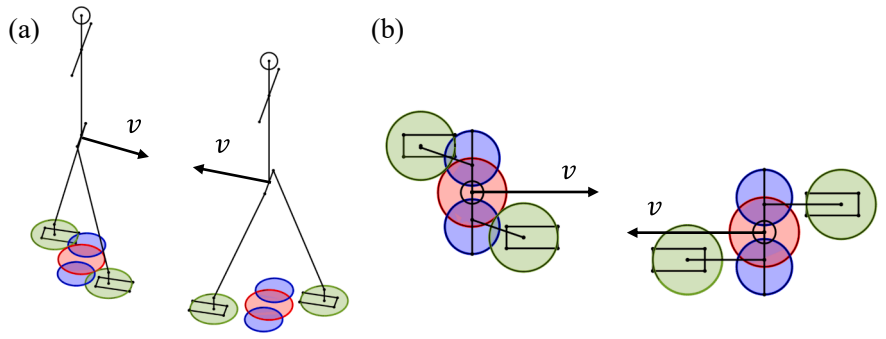

Fig. 10. Collision avoidance model tracking feet and torso over time using five circles: (a) lateral view; (b) superior view.

bidirectional flow. The stratification degree of bidirectional flow is typically measured using the order parameter. In experiments conducted by Murakami et al. (2021), two groups of 27 pedestrians each walked in opposite directions through a corridor. The study included three experimental conditions and one baseline condition. In the experimental conditions, some pedestrians in three different positions (front, middle, and rear) were distracted by using mobile phones, whereas in the baseline condition, no pedestrians were distracted. Each condition was replicated 12 times. The order parameter was calculated from open-source trajectory data. For the analysis in the current paper, only the 12 sets of trajectories from the baseline condition are utilized and are denoted as *LFE*.

Fundamental diagram: The experimental data for the fundamental diagram are obtained from Jin et al. (2021) and were determined from experiments conducted in circular corridors with different widths (W = 2.5, 2, 1.5, and 1 m). Pedestrians were randomly positioned at the start and evenly divided into two groups. One group was instructed to walk in one direction, and the other group was instructed to walk in the opposite direction. After lanes were formed, data on the local density and local flow rate were collected. The local density ranged from 1 to 11 ped/m^2. In this section, this dataset is denoted as *FDE*.

3.2. Simulation setup

Three models are tested in this paper: the HPM, the SF model (Helbing et al., 2000), and the heuristic-based model (Moussaïd et al., 2011). In the SF model and the heuristic-based model, pedestrians are represented as circles. In contrast, the HPM represents pedestrians using a three-circle configuration with a total area of approximately 0.88 m^2 for gait parameter calculations. To maintain consistency in the areal representation, the radius of the circle in the SF and the heuristic-based models is set to 0.168 m.

The simulations replicate the following experimental conditions.

Individual trajectories: The initial positions of two pedestrians are set to match the starting points obtained from the experimental trajectories. In the HPM, the pedestrians begin walking with a randomly chosen foot, and their target directions are aligned with the corridor. As the pedestrians pass each other, their target directions are adjusted toward the endpoints of their respective experimental trajectories. Each of 120 pairs undergoes 100 simulations, and the trajectory with the smallest average error, i.e., the smallest deviation from the experimental trajectory (for details, see Appendix B), is selected as the simulation result.

Lane formation process: The simulation corridor is depicted in Fig. 11 (a) and (b) and is identical to the corridor used in the

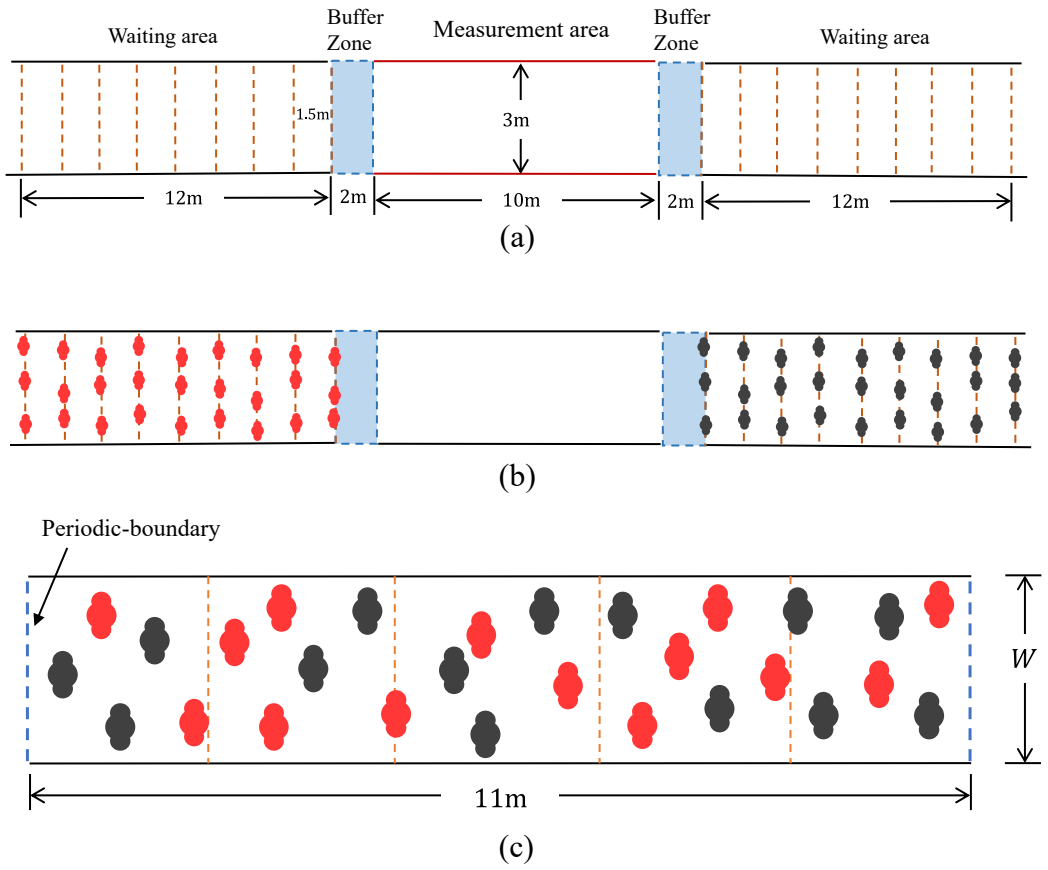

Fig. 11. Illustration of the simulation setup: (a) and (b) Lane formation task, where pedestrians are randomly positioned in the waiting lanes (three per line). (c) Fundamental diagram task, where pedestrians are randomly positioned in the periodic-boundary corridor. Pedestrians colored red move to the right, while those colored black move to the left.

experiment. It consists of three sections: a measurement area (10 m × 3 m), two buffer zones (2 m × 3 m), and two waiting areas (12 m × 3 m), each containing nine starting lines. The 54 pedestrians are divided into two groups of 27 pedestrians and then randomly positioned on one of the nine starting lines in each waiting area, with three pedestrians per line. The target directions of all pedestrians are aligned with the corridor. As in the experiment, the simulations are conducted over 12 runs, each lasting 30 s, with each run starting from a random initial position.

Fundamental diagram: Two equal-sized groups of pedestrians are randomly initialized in a straight corridor (11 m × W) with periodic boundaries, as illustrated in Fig. 11(c). These boundaries enable pedestrians to reenter the corridor from the opposite side.

In the experiments (Jin et al., 2021), there were no physical barriers restricting upper-body movements and thus shoulders could extend beyond the circular corridors. In contrast, the simulations constrain all pedestrians to walk within the corridor. Hence, to deal with the difference between the experiments and simulations, W in the simulations is set to be 0.2 m larger than W in the experiments.

The measurement area is divided equally into five subareas to calculate local density and local flow rate. The pedestrian number ranges from N = 10 to N = 110, with an interval of 10 in the simulation. Each run begins from a random initial position. Data are collected after the lane formation processes have stabilized.

4. Simulation results

The calibration results for the HPM are presented in Appendix C, while Appendix D provides an overview of the social force and heuristic-based models and their respective parameters.

4.1. Results for individual trajectories

Fig. 12 shows the average error ERR^{ave} and the maximum error ERR^{max} for each pair of trajectories, as determined by comparison with the experimental results *TrajE*. Table 2 lists the overall average error and the overall maximum error for the three models. The results indicate that the HPM outperforms the other two models on almost all pairs of trajectories. The SF model exhibits the largest deviations, as illustrated by the trajectory patterns in Fig. 13. Pedestrians controlled by the SF model initially walk toward each other at a constant velocity and in a fixed direction. When they are very close to each other, there is a sudden increase in repulsive force that causes them to perform abrupt and larger-than-90° turns, which is highly unrealistic. The heuristic-based model enables pedestrians to change direction in advance to avoid collisions, even when they are at a considerable distance from each other. Thus, the heuristic-based model has smoother trajectories than the SF model. However, the HPM exhibits an average deviation that is approximately 33.3 % smaller than that of the heuristic-based model, indicating that the HPM generates more realistic trajectories than the heuristic-based model.

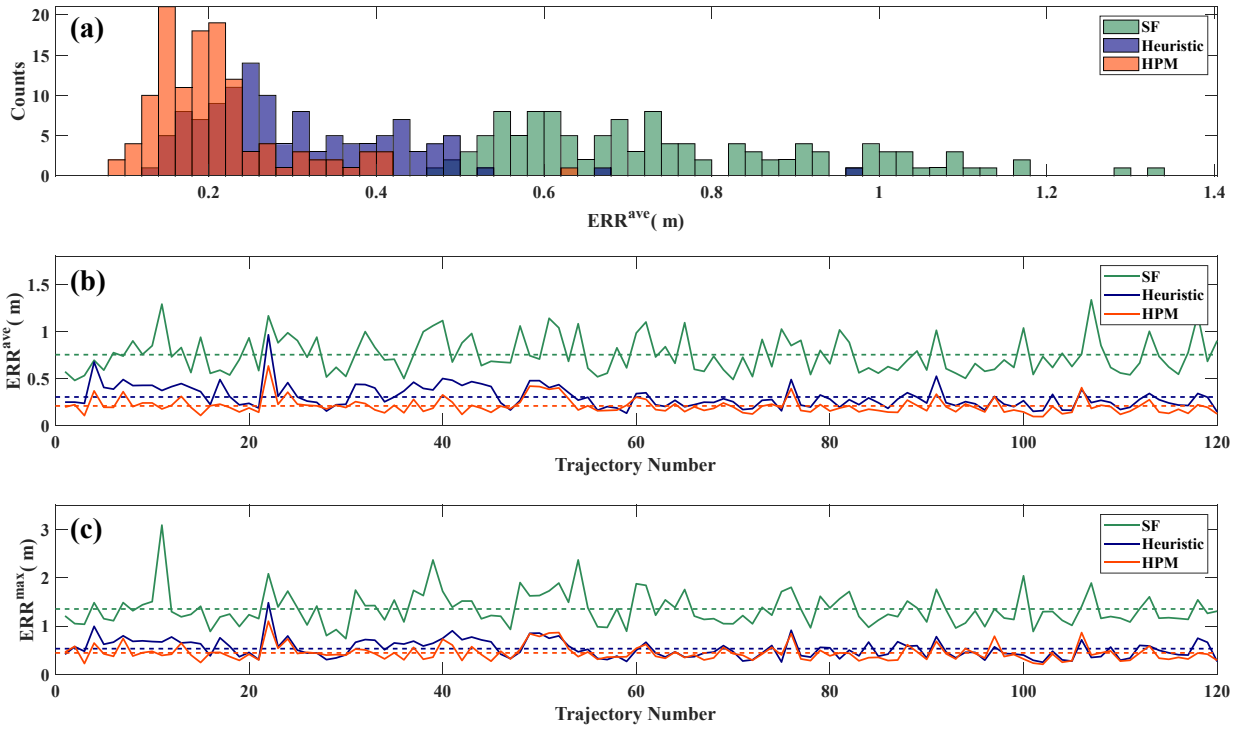

Fig. 12. (a) Distribution of the mean deviation. The mean deviation (b) and the maximum deviation (c) for each pair of trajectories.

Table 2
Experimental and simulation results in two scenarios.

	Trajectory		Lane formation
	ERR^{ave}(m)	ERR^{max}(m)	Onset (s)
Experiment	–	–	4.478 ± 1.145
HPM	0.208 ± 0.081	0.445 ± 0.160	4.975 ± 0.722
Heuristic-based	0.303 ± 0.122	0.531 ± 0.192	16.596 ± 10.473
SF	0.753 ± 0.194	1.353 ± 0.347	29.733 ± 0.924

Note: The results are means ± standard deviations.

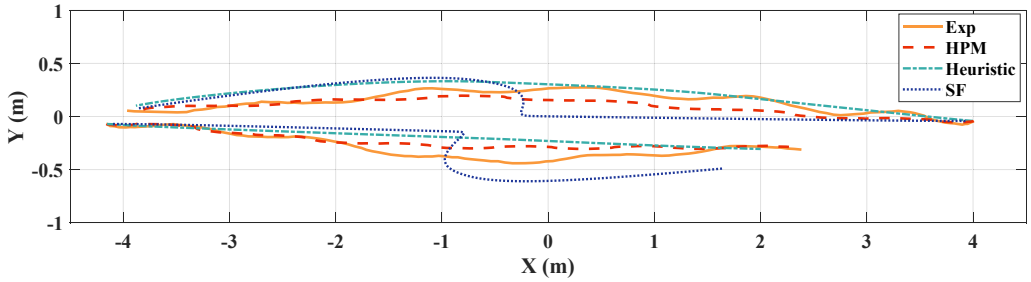

Fig. 13. The 101st pair of trajectories of *TrajE*, and the corresponding model-simulated trajectories.

4.2. Lane formation process

The self-organization process of bidirectional flow can be divided into two phases, i.e., a phase before lane formation and a phase after lane formation. The stratification degree of the flow can be measured using the order parameter Φ (Murakami et al., 2021), which is defined by the following equations:

$$\varphi_j(t) = \left(\frac{n_j^R - n_j^L}{n_j^R + n_j^L}\right)^2 \tag{17}$$

$$\Phi(\mathrm{t}) = \frac{1}{N}\sum_{j=1}^{N}\varphi_j(t) \tag{18}$$

where N is the number of rows along the corridor, discretized into 0.2 m × 0.2 m cells, and the subindex j indicates the j th row. The local order parameter in the j th row at time t, $\varphi_j(t)$, is calculated according to the number of pedestrians walking to the right (n_j^R) or to the left (n_j^L) in the j th row. The global order parameter $\Phi(t)$ is obtained by averaging $\varphi_j(t)$ across N rows.

Specifically, $\Phi(t) = 0$ when there are no pedestrians in the corridor or when there is completely mixed bidirectional flow. For perfectly aligned bidirectional flow, in which each row is occupied by at least one pedestrian, Φ reaches 1. The time at which $\Phi(t)$ first exceeds 0.8 after the first pedestrian enters the measurement area is considered to be evidence of lane formation (Murakami et al., 2021) and thus this moment is regarded as the onset of lane formation. During 12 simulation runs with the heuristic-based and SF model, deadlock situations are observed. Therefore, the onset of lane formation is set to the simulation time in such cases, i.e., 30 s. Fig. 14 and Table 2 describe the onset of lane formation and the statistical results in both experiments (*LFE*) and three models. It can be seen that the onset of lane formation in the HPM agrees well with the empirical data.

Furthermore, the parameter $\Phi(t)$ varies over time, reflecting the evolution of lane formation. Fig. 15(a)–(c) illustrates the time development of $\Phi(t)$ for a single run of the HPM, the SF model, and the heuristic-based model, compared with the experimental results, i.e., *LFE*. Fig. 15(d)–(f) contains the average results across 12 runs. It is evident that the HPM more closely agrees with *LFE* in terms of the evolution of $\Phi(t)$ than the other two models, indicating that pedestrians controlled by the HPM follow a lane formation process that is similar to that observed in the experiments.

Additional evidence is provided by snapshots of the lane formation process. As depicted in Fig. 16, in the HPM, pedestrians entering the measurement area naturally form lanes via a process that involves body rotation. In contrast, in the heuristic-based model, the lane formation process is significantly delayed. This may be due to pedestrians being regarded as circles and body rotation not being allowed. Specifically, when the two groups of pedestrians enter the measurement area, the pedestrians start to adjust their walking direction by exploring a collision-free direction. However, if the gap between two pedestrians moving in the opposite direction to a third pedestrian or the gap between the one pedestrian and the wall is smaller than each pedestrian's body size (2 × 0.168 m = 0.336 m), the third pedestrian does not choose to pass between the two other pedestrians or walk along the wall. Instead, the third pedestrian either waits for the two other pedestrians to adjust their direction to create a passable gap or finds another collision-free direction. This

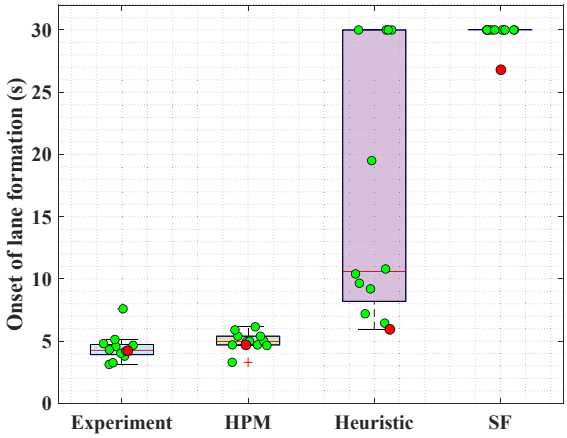

Fig. 14. Comparison of onset of lane formation between *LFE* and three models.

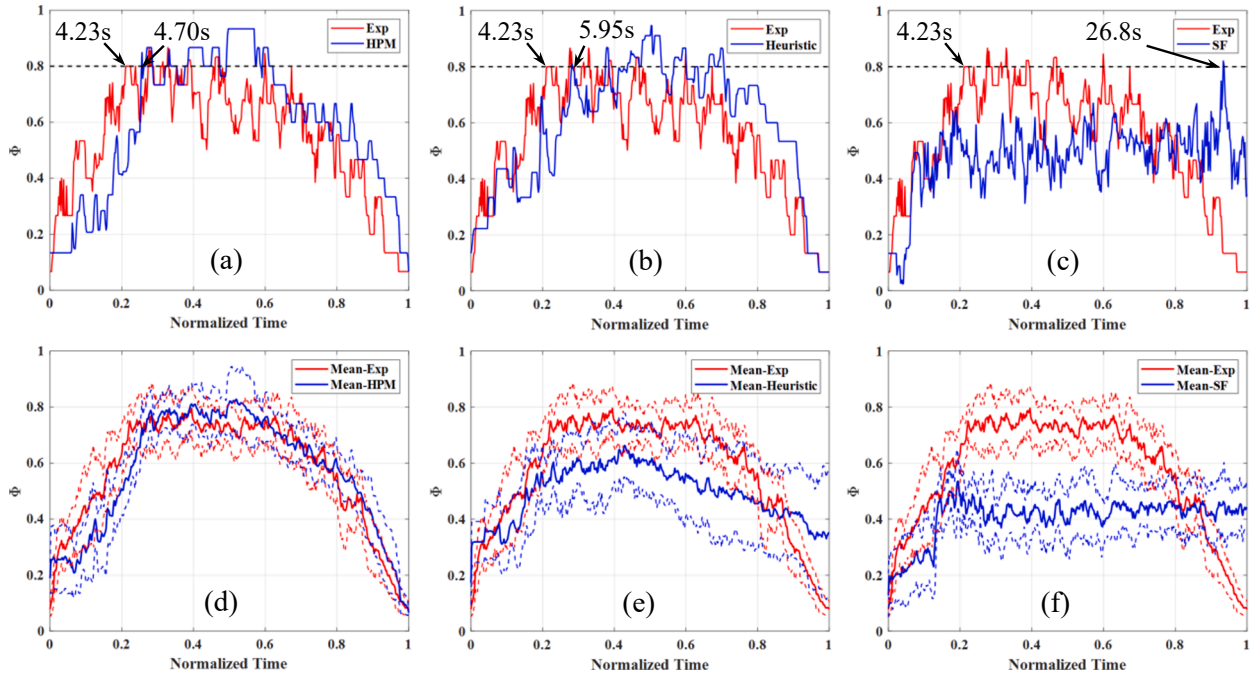

Fig. 15. Evolution of the order parameter Φ. The time, recorded from when the first pedestrian enters the measurement area until the last one exits this area, is normalized to range from 0 to 1. Red line: *LFE*; blue line: simulation result. (a)–(c) Examples of single trials that correspond to the red dots in Fig. 14. (d)–(f) Average results across 12 runs. The dashed lines show the means ± standard deviations of Φ. (a),(d) HPM vs. *LFE*; (b),(e) the heuristic-based model vs. *LFE*; and (c),(f) the SF model vs. *LFE*.

results in a delayed lane-formation process.

The above-mentioned problem is effectively resolved in the HPM. That is, even though the pedestrians in the HPM have a larger shoulder width (0.45 m) than those in other models, the pedestrians in the HPM can rotate their bodies to pass through a narrow gap, provided that its width is greater than their body depth ($2R_S = 0.25m$).

4.3. Fundamental diagram

In Jin et al. (2019, 2021), local density in an area is defined as follows:

$$\rho_l = \frac{1}{\Delta t}\int_t^{t+\Delta t} \frac{N_l(t)}{s} dt \tag{19}$$

Thus, the corridor is equally divided into five subareas, as shown in Fig. 11(c). $N_l(t)$ is the number of pedestrians in one subarea at

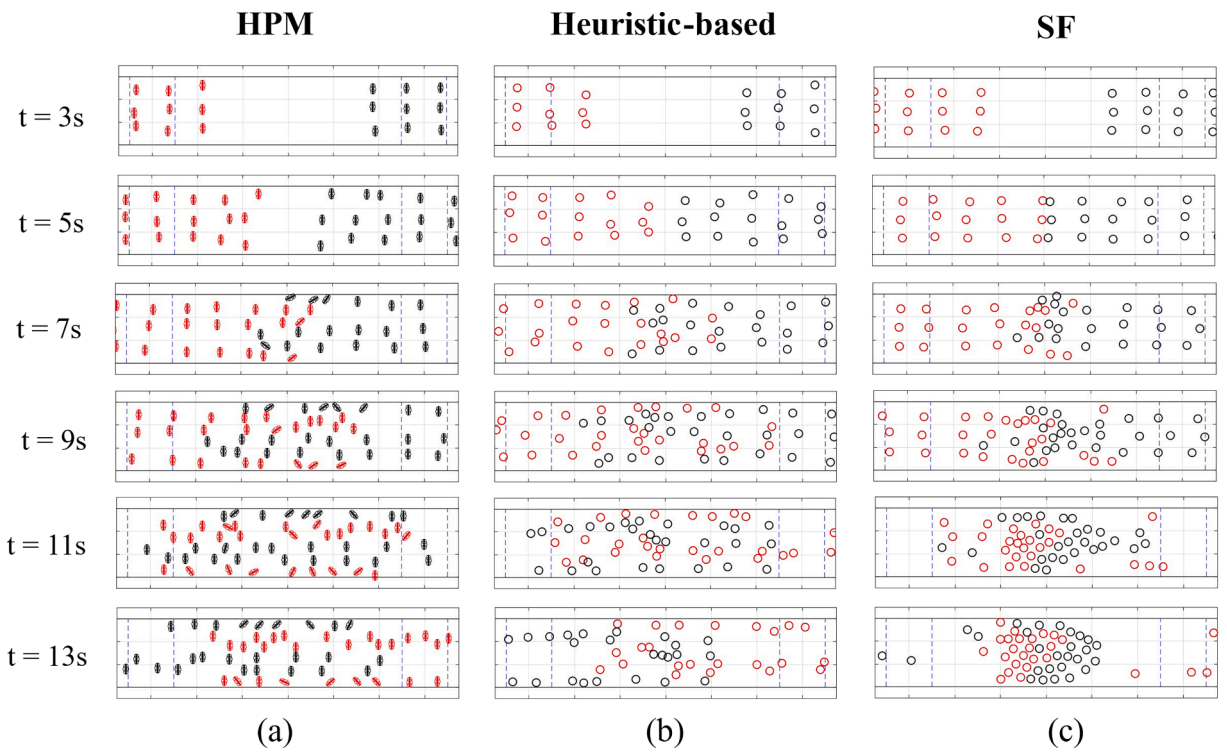

Fig. 16. Snapshots of lane formation process in (a) the HPM; (b) the heuristic-based model; and (c) the SF model. These snapshots are taken from the trials that are marked by the red dots in Fig. 14 and Fig. 15(a)–(c).

time t; s is the size of each subarea, which is 4.4 m^2; and Δt is set to 5 s.

The corresponding local flow rate is defined as $f_l = \frac{q}{W\Delta t}$, where q is the number of pedestrians crossing the subarea per unit of time (Δt); W is the corridor width.

Fig. 17(a) shows the gridlock probability for the three models under different global densities. For simulations in which gridlock does not occur, the results from five runs under each pedestrian number condition are plotted in the fundamental diagrams illustrated in Fig. 17 (b) and (c). It is evident that compared with the outcomes of the SF and heuristic-based models, those of the HPM are significantly better, illustrated by local densities ranging from 0.5 to 7 ped/m^2. Moreover, error terms (detailed in Appendix B) quantify the discrepancies between the HPM and *FDE*. These comprise the mean squared error, root-mean-square error, relative root-mean-square error, and mean absolute percentage error, which have values of 0.0247, 0.1572, 15.48 %, and 18.79 %, respectively, demonstrating strong alignment between the results of the HPM and *FDE*.

Moreover, several snapshots depicted in Fig. 18 (a)–(h) show the evolution of bidirectional flow. The transition from a disordered, randomized flow to a stable, well-aligned flow indicates that the HPM performs effectively in representing short-term collision

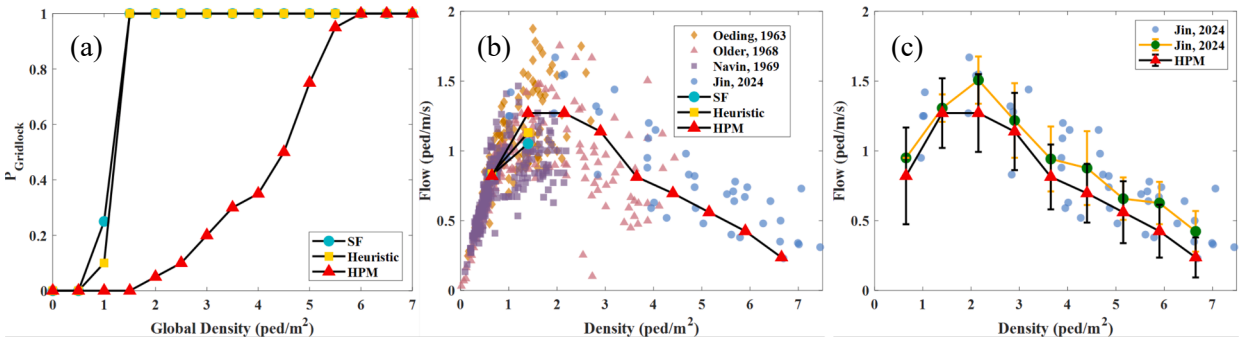

Fig. 17. (a) Relationship between gridlock probability and global density. (b) Fundamental diagram containing scatter points, which are experimental data (Navin and Wheeler, 1969; Oeding, 1963; Older, 1968) and *FDE*; and solid lines, which are the results of the three models after binning processing (Jelić et al., 2012). (c) Fundamental diagram containing scatter points, which are *FDE*; an orange line, which represents the results after binning; and a black line, which represents the results of the HPM.

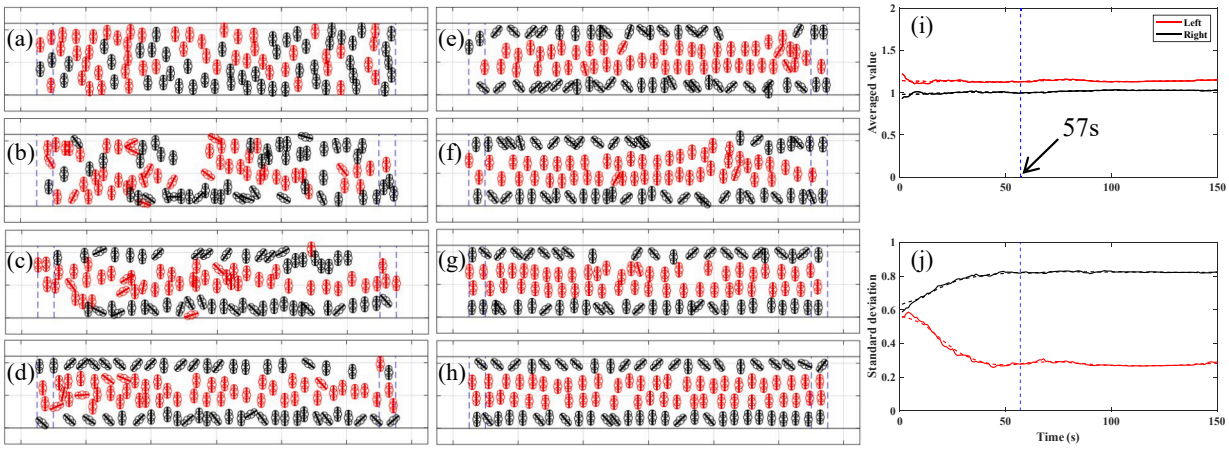

Fig. 18. Snapshots of simulations by the HPM with 100 pedestrians ($\rho_{Global} \approx 5\,\text{ped}/\text{m}^2$) at (a) 0 s; (b) 10 s; (c) 25 s; (d) 40 s; (e) 55 s; (f) 70 s; (g) 90 s; and (h) 130 s. Pedestrians colored red (black) walk leftward (rightward). (i), (j) The evolution of the means and standard deviations, respectively, of the *y*-coordinates for all pedestrians. Solid red and black lines represent the pedestrians moving to the left and right, respectively. The dashed lines are the smoothed results of the corresponding solid lines.

avoidance during the initial stage of lane formation. Once the lanes are established, body rotation further helps to reduce head-on conflicts. The time required to form stable lanes is 57 s, which is very close to the result in Jin et al. (2021) (see Fig. 18 (i) and (j)).

5. Conclusions

This paper addresses bidirectional flow, which is a classic scenario in pedestrian dynamics. The HPM is enhanced by integrating two distinct gait types and introducing a novel gait-planning process. The two gaits—walking while rotating and walking while turning—capture the complexities of human walking behavior, emphasizing the relationship between rotational or turning direction and the supporting foot. A novel energy-based heuristic rule is proposed to encompass three cost forms for step execution: deviation from the target direction, body rotation to navigate narrow gaps, and reduced walking velocity. This energy-based heuristic rule determines the optimal avoidance direction and body rotation angle without the need for parameter calibration. This approach supports the concept that pedestrians choose their movement direction by minimizing mechanical energy consumption.

Simulations are performed to test the improved HPM against experimental results and two established models—the heuristic-based model and the SF model. Our findings make key contributions to the field in the following three areas. 1) **Individual trajectories**: The trajectories simulated by the improved HPM closely match experimental data, showing less deviation than the trajectories simulated by other models. 2) **Lane formation**: The improved HPM effectively reproduces the lane formation process, with body rotations that facilitate efficient lane formation. The onset of lane formation and the evolution of the order parameter align well with experimental data. 3) **Fundamental diagram**: The improved HPM exhibits a swift transition from randomized flow to a stable, well-ordered flow, demonstrating its effective simulation of bidirectional flow. Moreover, the maximum density reaches 7 ped/m^2, representing a marked improvement compared with continuum-space models.

While the HPM possesses more parameters and entails a complex setup compared to simpler models like the SF and heuristic-based models, it outperforms in two key aspects. First, it strikes a balance between accuracy and complexity (refer to Appendix F). Second, the runtime is comparable to that of existing models in the literature (see Appendix G). These factors demonstrate that, despite appearing complex, the HPM is still practical for use. Furthermore, the HPM is anticipated to introduce new approaches and provide inspiration to the field of crowd animations.

However, while the improved HPM demonstrates effective simulation capabilities in bidirectional flow scenarios, it nevertheless faces challenges in simulating high-density crowds (> 7 ped/m^2), especially when the initial positioning of pedestrians is random. This limitation arises due to complex interactions (e.g., physical contacts and compressions between pedestrians and between pedestrians and walls), which are difficult to accurately characterize using our proposed heuristic rules. In future work, the aim will be to further enhance the improved HPM by incorporating data on compression pressures observed in high-density crowds. This approach will afford an even better HPM, which will be capable of simulating high-density crowds more realistically than the improved HPM, thereby improving the understanding of crowd dynamics.

CRediT authorship contribution statement

Xiaoyun Shang: Writing – review & editing, Writing – original draft, Visualization, Validation, Software, Methodology, Formal analysis, Data curation. **Rui Jiang:** Writing – review & editing, Writing – original draft, Supervision, Methodology, Formal analysis, Conceptualization. **S.C. Wong:** Writing – review & editing, Writing – original draft, Methodology, Funding acquisition, Conceptualization. **Ziyou Gao:** Funding acquisition, Conceptualization. **Wenguo Weng:** Writing – review & editing, Formal analysis.

Declaration of competing interest

The authors declare that they have no known competing financial interests or personal relationships that could have appeared to influence the work reported in this paper.

Acknowledgments

This work described in this paper was supported by grants from the National Natural Science Foundation of China (Project Nos. W2411064, 72288101 and 71931002), and a grant from the Research Grants Council of the Hong Kong Special Administrative Region, China (Project No. 17202824). The third author was also supported by Francis S Y Bong Professorship in Engineering.

Appendix A. Joint rotation angles

Table A1 and Table A2 list the joint rotation angle values for gait G_R, where L (R) indicates the left (right) foot support scenario, and l_i^F represents the l^F of pedestrian i. As noted in Shang et al. (2024), the maximum pelvis rotation angle ψ_p^{max} should be limited. Additionally, the joint rotation angle values for gait G_T are listed in Table A3 and Table A4. L^p is the pelvis width and L^l is the leg length, which are equivalent to L_3 and L_2 (L_4), respectively, in Fig. 2(b).

Table A1
Values of Euler angles for ped_i in the three walking states of gait G_R.

Parameter	Value		
	N	E	D
R^{max}	l_i^F	$l_i^F + L_i^{p'}$	$l_i^F - L_i^{p'}$
ψ_P	0	$\min\left(\psi_P^{max}, \frac{\pi}{2} - \theta\right)$	$\min\left(\psi_P^{max}, \frac{\pi}{2} - \theta\right)$
ψ_S	0	$\frac{\pi}{2} - \theta$	$\frac{\pi}{2} - \theta$
θ_R	$\arcsin\left(\frac{l}{2L^l}\right)$	$\arcsin\left(\frac{l - L^{p\prime}}{2L^l}\right)$	$\arcsin\left(\frac{l + L^{p\prime}}{2L^l}\right)$

Note: $L^{p'} = L^p \sin\psi_p$ denotes the projection of the pelvis in the target direction γ.

Table A2
Values of joint rotation angles for gait G_R.

θ	Value	φ	Value (L)	Value (R)	ψ	Value
θ_1	θ_R	φ_1	$-\omega$	ω	ψ_1	ψ_p
θ_2	$-\theta_R$	φ_2	0	0	ψ_2	$-\psi_p$
θ_3	$-\theta_R$	φ_3	$\pi/2$	$-\pi/2$	ψ_3	$\psi_S - \psi_p$
θ_4	θ_R	φ_4	ω	$-\omega$	—	—

Table A3
Values of Euler angles for ped_i in the three walking states of gait G_T.

Parameter	Value		
	N	E	D
R^{max}	l_i^F	l_i^F	l_i^F
ψ_T	0	$\arcsin\left(\frac{L^p - w}{2L^l}\right)$	$\arcsin\left(\frac{L^p - w}{2L^l}\right)$
θ_T	$\arcsin\left(\frac{l}{2L^l}\right)$	$\arcsin\left(\frac{l}{2L^l}\right)$	$\arcsin\left(\frac{l}{2L^l}\right)$

Table A4
Values of joint rotation angles for gait G_T.

θ	Value	φ	Value (L)	Value (R)	ψ	Value
θ_1	θ_T	φ_1	$-\psi_T-\omega$	$\psi_T+\omega$	ψ_1	0
θ_2	$-\theta_T$	φ_2	ψ_T	ψ_T	ψ_2	0
θ_3	$-\theta_T$	φ_3	$\pi/2+\psi_T$	$-\pi/2-\psi_T$	ψ_3	0
θ_4	θ_T	φ_4	ω	$-\omega$	—	—

Although Gimbal lock, which occurs when two rotation axes become aligned—typically when the pitch angle (denoted as "φ" in Fig. 2(b)) reaches $\pm 90^{\circ}$, is often observed in the model with Euler angles, we did not consider it in our simulations. This is because this extreme angle corresponds to a cross-split motion, a scenario that does not occur during normal walking.

Appendix B. Definition of error terms

Error terms are used to compare the differences between the experiment and the simulation in terms of trajectories and flow–density relationships.

The average error for the i-th pair of trajectories is defined as the average of the errors between the i-th pair of experimental and simulated trajectories at each moment, as follows:

$$ERR_i^{ave} = \frac{1}{2N}\sum_{j=1}^{2}\sum_{t=1}^{N}\left\|P_{i,j}^{exp}(t) - P_{i,j}^{sim}(t)\right\| \tag{B.1}$$

The maximum error for the i-th pair of trajectories is defined as the maximum of the errors between the i-th pair of experimental and simulated trajectories at each moment, as follows:

$$ERR_i^{max} = \max_{t\in\{1,2,\ldots,N\};j\in\{1,2\}}\left(\left\|P_{i,j}^{exp}(t) - P_{i,j}^{sim}(t)\right\|\right) \tag{B.2}$$

where i is the i-th pair of trajectories; N is the total number of frames, each of which correspond to $1/20$ s (Murakami et al., 2022); j is one trajectory within a pair; and $P_{i,j}^{exp}(t)$ ($P_{i,j}^{sim}(t)$) is the position of a pedestrian at time t in the j-th trajectory of the i-th pair of experimental (simulated) trajectories.

Error terms for the flow–density relationship, such as the mean square error (MSE), root-mean-square error (RMSE), relative root-mean-square error (RRMSE), and mean absolute percent error (MAPE), are calculated as follows:

$$MSE = \frac{1}{N}\sum_{i=1}^{N}\left(y_i^{exp} - y_i^{\mathrm{sim}}\right)^2 \tag{B.3}$$

$$RMSE = \sqrt{\frac{1}{N}\sum_{i=1}^{N}\left(y_i^{exp} - y_i^{\mathrm{sim}}\right)^2} \tag{B.4}$$

$$RRMSE = \frac{\sqrt{\frac{1}{N}\sum_{i=1}^{N}\left(y_i^{exp} - y_i^{\mathrm{sim}}\right)^2}}{\sqrt{\frac{1}{N}\sum_{i=1}^{N}\left(y_i^{exp}\right)^2}} \tag{B.5}$$

$$MAPE = \frac{1}{N}\sum_{i=1}^{N}\left|\frac{y_i^{exp} - y_i^{\mathrm{sim}}}{y_i^{exp}}\right| \tag{B.6}$$

where y_i^{exp} (y_i^{sim}) is the experimental (simulated) average flow rate at the i-th density interval, and N is the total number of density intervals.

Appendix C. Model calibration

The pedestrian height H is a random number in the interval [1.6, 1.8] (m). The body depth is calculated as $0.25/1.7H$ and has an average value of 0.25 m. The selection of the moments of inertia J_{C1} and J_{C2} is based on the inertia parameters of the adult human body provided by the China National Standard (GB/T 17245–2004) and the data presented in Song et al. (2019). The free-walking step length l^F is within [0.6, 0.75] (m), and the free-walking velocity is within [1.2, 1.5] (m/s). The four parameters of step duration (T^0, T^{upp}, β_1, and β_2) are the same as those used by Shang et al. (2024).

The genetic algorithm is employed to calibrate other parameters, with the aim of minimizing the mean squared error (as defined in Appendix B) between the experimental and simulated local flow rates. A summary of all calibrated parameters in the HPM is provided in Table C1.

Table C1
Parameter values used in the simulations.

Parameter	Definition	Value	Unit
H	Pedestrian height	$[1.6, 1.8]$	m
M	Pedestrian mass	$[50, 65]$	kg
R_l	Thigh radius	$[0.07, 0.09]$	m
J_{C1}	Moment of inertia	$[7, 9.4]$	$\mathrm{kg\,m^2}$
J_{C2}	Moment of inertia	4	$\mathrm{kg\,m^2}$
ψ_p^{max}	Maximum pelvis rotation angle	$\pi/4$	rad
ω_0	Maximum sway angle	$\pi/180$	rad
D^v	Vision limitation	$[6, 10]$	m
κ_1	Parameter of penalty function $\mathscr{F}$	0.05	–
κ_2	Parameter for safety insurance	0.8	–
κ_3	Parameter of gait selection	0.05	rad
T^0	Minimum step duration	0.5	s
T^{upp}	Upper bound of step duration	0.8	s
β_1	Parameter of step duration	0.15	–
β_2	Parameter of step duration	0.25	–
δ	Time step	0.05	s

A discussion on the determination of the time step δ is presented in Appendix E.

Appendix D. Social force model and heuristic-based model

The details of the modified social force model in this paper are as follows.

Firstly, the self-driven force, $\vec{f}_i^s$, is defined as $\vec{f}_i^s = m_i\left(v_i^0\vec{e}_i^0 - \vec{v}_i\right)/\tau$, where v_i^0 denotes desired speed and $\vec{e}_i^0$ denotes desired direction. The actual velocity $\vec{v}_i$ changes with the relaxation time τ. m_i is the mass of ped_i.

The repulsive force $\vec{f}_{ij}$ between pedestrians i and j, and the repulsive force $\vec{f}_{iw}$ between pedestrians i and the wall w are determined as follows:

$$\vec{f}_{ij} = \begin{cases} A\exp\left[\dfrac{\left(r_{ij} - \left\|\vec{d}_{ij}\right\|\right)}{B}\right]\vec{n}_{ij} + g\left(r_{ij} - \left\|\vec{d}_{ij}\right\|\right)\left(K\vec{n}_{ij} + \kappa\Delta v_{ji}^t\vec{t}_{ij}\right), & \vec{v}_i \bullet \vec{v}_j \geq 0 \text{ and } \left\|\vec{d}_{ij}\right\| < D_v \\ g\left(r_{ij} - \left\|\vec{d}_{ij}\right\|\right)\left(k\vec{n}_{ij} + \kappa\Delta v_{ji}^t\vec{t}_{ij}\right), & \vec{v}_i \bullet \vec{v}_j < 0 \\ 0, \ otherwise \end{cases} \tag{D.1}$$

$$\vec{f}_{iw} = A\exp\left[\frac{\left(r_i - \left\|\vec{d}_{iw}\right\|\right)}{B}\right]\vec{n}_{iw} + g\left(r_i - \left\|\vec{d}_{iw}\right\|\right)K\vec{n}_{ij} \tag{D.2}$$

where, $g(x) = (|x| + x)/2$; $r_{ij} = r_i + r_j$ is the sum of the radius of the two pedestrians; $\|\vec{d}_{ij}\| = \|C_i - C_j\|$ is the distance between the centers of the two pedestrians; $\vec{n}_{ij}$ is the normal unit vector from pedestrian j to i; $\vec{t}_{ij}$ is the unit tangential vector; $\Delta v_{ji}^t = \left(\vec{v}_j - \vec{v}_i\right) \bullet \vec{t}_{ij}$ is the tangential velocity difference; $\|\vec{d}_{iw}\|$ is the vertical distance to the wall; $\vec{n}_{iw}$ is the unit normal vector from the wall to ped_i. D_v is the vision limitation distance; and A, B, K, and κ are constants.

The resulting acceleration equation is:

$$\frac{d\vec{v}_i}{dt} = \frac{1}{m_i}\left(\vec{f}_i^s + \sum\nolimits_j \vec{f}_{ij} + \sum\nolimits_w \vec{f}_{iw}\right) \tag{D.3}$$

The parameters are listed in the Table D1. A, B, K, κ are calibrated using the genetic algorithm to minimize the mean squared error (defined in Appendix B) of the local flow rate between experiments and simulations. Other parameters are pre-determined, aligned with Appendix C.

Table D1
Parameter values of the social force model used in the simulations.

Parameter	Definition	Value	Unit
m	Pedestrian mass	$[50, 65]$	kg
v^0	Desired velocity	[1.2, 1.5]	ms^{-1}
D_v	Vision limitation	$[6, 10]$	m
τ	Relaxation time	0.5	s
A	Parameter of social force	800	N
B	Parameter of social force	0.08	m
K	Parameter of social force	3000	$kg\,s^{-2}$
κ	Parameter of social force	5000	$m^{-1}kg\ s^{-2}$

The details of the heuristic-based model in this paper are exactly the same with the model in (Moussaïd et al., 2011).

The model parameters are listed in the Table D2. K is calibrated using the genetic algorithm to minimize the mean squared error (defined in Appendix B) of the local flow rate between experiments and simulations. Other parameters are pre-determined, aligned with Appendix C.

Table D2
Parameter values of the heuristic-based model used in the simulations.

Parameter	Definition	Value	Unit
m	Pedestrian mass	$[50, 65]$	kg
v^0	Desired velocity	[1.2, 1.5]	ms^{-1}
d_{max}	Vision limitation	$[6, 10]$	m
Φ	Boundary of the vision area	$\pi/2$	rad
τ	Relaxation time	0.5	s
K	Parameter of contact force	3000	$kg\ s^{-2}$

Appendix E. Determination of simulation time step

We utilize an open-boundary bi-directional flow scenario to investigate the influence of time step size (δ) on the onset of lane formation. Specifically, we test six time-step sizes: 1/10 s, 1/15 s, 1/20 s, 1/25 s, 1/30 s, and 1/35 s, which correspond to 10, 15, 20, 25, 30, and 35 frames per second, respectively. The results, depicted in Fig. E1, suggest that a relatively large time step (i.e., 1/10 s and 1/15 s) results in a significantly longer lane formation time compared to the experimental results. However, when the time step is 1/20 s or smaller, the onset of lane formation aligns closely with the experimental results, with no significant variations across the different time steps. Therefore, we select a time step size of 0.05 s for the simulations.

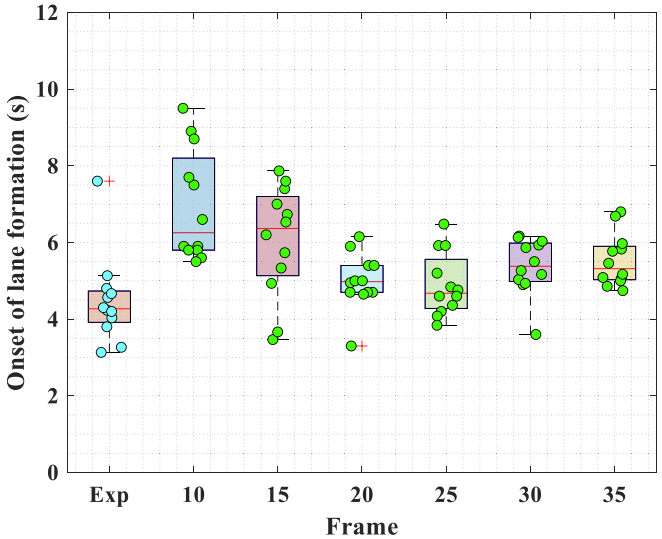

Fig. E1. Comparison of the onset of lane formation between experimental results and the HPM for different time steps (frames).

Appendix F. Comparison of the Akaike Information Criteria (AIC) metric among three models

We use the AIC metric to evaluate model performance by considering both the number of parameters and the simulation accuracy.

The AIC metric is calculated as follows:

$$AIC = 2k - \ln\widehat{L} \tag{F.1}$$

where k represents the number of parameters in the model,[1] which are 4, 5, and 12 for the heuristic-based model, the social force model, and the HPM, respectively. $\ln\widehat{L}$ denotes the natural logarithm of the likelihood function, indicating how well the model fits the experimental data. With the assumption that the residuals follow a normal distribution $N(0,\sigma^2)$, the log-likelihood is given as follows:

$$\ln\widehat{L} = -\frac{n}{2}\ln 2\pi - \frac{n}{2}\ln\sigma^2 - \frac{n}{2} \tag{F.2}$$

where n is the number of data points, and σ^2 is the variance of the residuals.

We evaluate the differences between the simulation results and experimental data for three models across two scenarios. The results are provided in Table F1.

Table F1
Results of the AIC metric.

	Heuristic	Social Force	HPM
Individual trajectory	81.8538	288.0651	4.6288
Onset of lane formation	110.1865	118.3111	44.6035

Appendix G. Comparison of the runtime among three models

We conducted a 20-second simulation, using the same time step for all three models and applying the same field-of-view discretization interval for both the HPM and the heuristic-based model. This simulation was repeated five times. Fig. G1 compares the runtimes of the three models. The HPM runs faster than the heuristic-based model.

This is understandable as the heuristic-based model calculates the velocity for the next step at every time step. In contrast, the HPM only performs gait planning calculations during the double support phase, which approximately occurs every 10 time steps. The computation of body joint positions involves fourth-order matrix multiplications, making the process computationally efficient. Therefore, despite the HPM''s apparent complexity, its runtime performance is not as slow as one might initially expect.

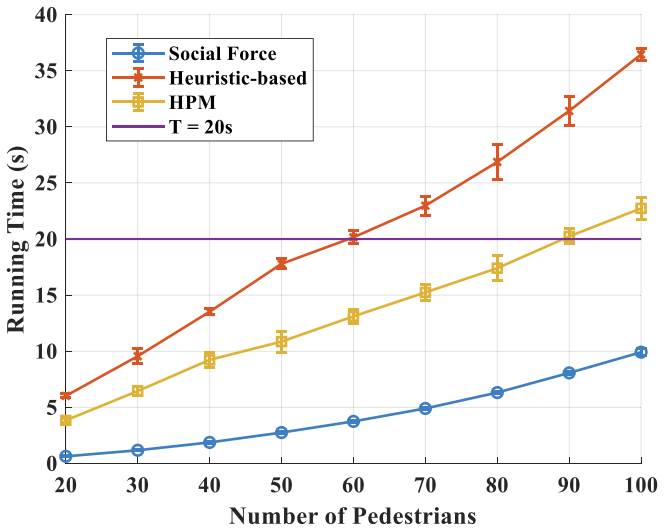

Fig. G1. Runtime comparison among the three models

[1] In this calculation, we do not consider the time step or the pedestrian's physical properties (i.e., body size, free-walking velocity, and mass) as model parameters, as these are not intrinsic to the model.

Data availability

Data will be made available on request.

References

Bacik, K.A., Bacik, B.S., Rogers, T., 2023. Lane nucleation in complex active flows. Science 379 (6635), 923–928.
Bandini, S., Mondini, M., Vizzari, G., 2014. Modelling negative interactions among pedestrians in high density situations. Transp. Res. Part C Emerging Technol. 40, 251–270.
Blue, V.J., Adler, J.L., 2001. Cellular automata microsimulation for modeling bi-directional pedestrian walkways. Transp. Res. B Methodol. 35 (3), 293–312.
Bruneau, J., Olivier, A.H., Pettré, J., 2015. Going Through, Going Around: A Study on Individual Avoidance of Groups. IEEE Trans. Vis. Comput. Graph. 21 (4), 520–528.
Chatagnon, T., Feldmann, S., Adrian, J., Olivier, A.H., Pontonnier, C., Hoyet, L., Pettré, J., 2024. Standing balance recovery strategies of young adults in a densely populated environment following external perturbations. Saf. Sci. 177, 106601.
Chatagnon, T., Olivier, A.H., Hoyet, L., Pettré, J., Pontonnier, C., 2023. Stepping strategies of young adults undergoing sudden external perturbation from different directions. J. Biomech. 157, 111703.
Chraibi, M., Seyfried, A., Schadschneider, A., 2010. Generalized centrifugal-force model for pedestrian dynamics. Phys. Rev. E 82 (4), 046111.
Chung, W., Kim, H., Yoo, Y., Moon, C.-B., Park, J., 2012. The detection and following of human legs through inductive approaches for a mobile robot with a single laser range finder. IEEE Trans. Ind. Electron. 59 (8), 3156–3166.
Ding, H., Wang, Q., Chen, J., Lo, J.T.Y., Ma, J., 2024. Investigating pedestrian stepping characteristics via intrinsic trajectory. Physica A 652, 130045.
Donelan, J.M., Kram, R., Kuo, A.D., 2001. Mechanical and metabolic determinants of the preferred step width in human walking. Proceedings. Biological Sciences 268 (1480), 1985–1992.
Fang, S., Jin, C.J., Jiang, R., Li, D., 2024. Simulating the bi-directional pedestrian flow under high densities by a floor field cellular automaton model. Physica A 638, 129626.
Faraji, S., Ijspeert, A.J., 2017. 3LP: A linear 3D-walking model including torso and swing dynamics. Int. J. Rob. Res. 36 (4), 436–455.
Farina, F., Fontanelli, D., Garulli, A., Giannitrapani, A., Prattichizzo, D., 2017. Walking ahead: the headed social force model. PLoS One 12 (1), e0169734.
Feldmann, S., Adrian, J., 2023. Forward propagation of a push through a row of people. Saf. Sci. 164, 106173.
Feliciani, C., Nishinari, K., 2016. Empirical analysis of the lane formation process in bidirectional pedestrian flow. Phys. Rev. E 94 (3), 032304.
Feliciani, C., Nishinari, K., 2018. Measurement of congestion and intrinsic risk in pedestrian crowds. Transp. Res. Part C Emerging Technol. 91, 124–155.
Fu, Z., Xiong, X., Luo, L., Yang, Y., Feng, Y., Chen, H., 2022. Influence of rotation on pedestrian flow considering bipedal features: Modeling using a fine discrete floor field cellular automaton. Physica A 605, 128027.
Gu, F., Guiselin, B., Bain, N., Zuriguel, I., Bartolo, D., 2025. Emergence of collective oscillations in massive human crowds. Nature 638, 112–119.
Guo, N., Hao, Q.Y., Jiang, R., Hu, M.B., Jia, B., 2016. Uni- and bi-directional pedestrian flow in the view-limited condition: Experiments and modeling. Transp. Res. Part C Emerging Technol. 71, 63–85.
Guo, N., Jiang, R., Hao, Q.Y., Hu, M.B., Jia, B., 2019. Impact of holding umbrella on uni- and bi-directional pedestrian flow: experiments and modeling. Transportmetrica B 7 (1), 897–914.
Guy, S.J., Chhugani, J., Curtis, S., Dubey, P., Lin, M., Manocha, D., 2010. PLEdestrians: A least-effort approach to crowd simulation. Computer Animation 2010 - ACM SIGGRAPH / Eurographics Symposium Proceedings. SCA 2010, 119–128.
Helbing, D., Buzna, L., Johansson, A., Werner, T., 2005. Self-organized pedestrian crowd dynamics: Experiments, simulations, and design solutions. Transp. Sci. 39 (1), 1–24.
Helbing, D., Farkas, I., Vicsek, T., 2000. Simulating dynamical features of escape panic. Nature 407 (6803), 487–490.
Hoogendoorn, S., Daamen, W., 2005. Self-organization in pedestrian flow. Traffic and Granular Flow 2003, 373–382.
Huang, Z., Chraibi, M., Song, W., 2018. Simulation of pedestrian single-lane movement by a biped model. Phys. Rev. E 98 (4), 042309.
Jelić, A., Appert-Rolland, C., Lemercier, S., Pettré, J., 2012. Properties of pedestrians walking in line: Fundamental diagrams. Phys. Rev. E 85, 036111.
Jin, C.J., Jiang, R., Liu, T., Li, D., Wang, H., Liu, X., 2021. Pedestrian dynamics with different corridor widths: Investigation on a series of uni-directional and bi-directional experiments. Physica A 581, 126229.
Jin, C.J., Jiang, R., Wong, S.C., Xie, S., Li, D., Guo, N., Wang, W., 2019. Observational characteristics of pedestrian flows under high-density conditions based on controlled experiments. Transp. Res. Part C Emerging Technol. 109, 137–154.
Jin, C.J., Jiang, R., Yin, J.L., Dong, L.Y., Li, D., 2017. Simulating bi-directional pedestrian flow in a cellular automaton model considering the body-turning behavior. Physica A 482, 666–681.
Jindrich, D.L., Qiao, M., 2009. Maneuvers during legged locomotion. Chaos 19 (2), 026105.
Kajita, S., Hirukawa, H., Harada, K., Yokoi, K., 2014. Introduction to Humanoid Robotics. Springer Tracts. Adv. Rob. 101.
Kubo, M., Holt, K.G., Saltzman, E., Wagenaar, R.C., 2006. Changes in axial stiffness of the trunk as a function of walking speed. J. Biomech. 39 (4), 750–757.
Kuo, A.D., 1999. Stabilization of lateral motion in passive dynamic walking. Int. J. Rob. Res. 18 (9), 917–930.
Liang, H., Du, J., Wong, S.C., 2021. A continuum model for pedestrian flow with explicit consideration of crowd force and panic effects. Transp. Res. B Methodol. 149, 100–117.
Singh, S., Kapadia, M., Reinman, G., Faloutsos, P., 2011. Footstep navigation for dynamic crowds. Comput. Anim. Virtual Worlds 22, 271–281.
Ma, Y., Lee, E.W.M., Shi, M., Yuen, R.K.K., 2021. Spontaneous synchronization of motion in pedestrian crowds of different densities. Nat. Hum. Behav. 5 (4), 447–457.
Miyagawa, D., Ichinose, G., 2020. Cellular automaton model with turning behavior in crowd evacuation. Physica A 549, 124376.
Moussaïd, M., Helbing, D., Theraulaz, G., Materials, S.I., 2011. How simple rules determine pedestrian behavior and crowd disasters. Proc. Natl. Acad. Sci. 108 (17), 6884–6888.
Murakami, H., Feliciani, C., Nishinari, K., 2019. Lévy walk process in self-organization of pedestrian crowds. J. R. Soc. Interface 16, 20180939.
Murakami, H., Feliciani, C., Nishiyama, Y., Nishinari, K., 2021. Mutual anticipation can contribute to self-organization in human crowds. Sci. Adv. 7, eabe7758.
Murakami, H., Tomaru, T., Feliciani, C., Nishiyama, Y., 2022. Spontaneous behavioral coordination between avoiding pedestrians requires mutual anticipation rather than mutual gaze. Iscience 25 (11), 105474.
Navin, P., Wheeler, R., 1969. Pedestrian flow characteristics. Traffic. Engineering 19, 30–33.
Nikolić, M., Bierlaire, M., De Lapparent, M., Scarinci, R., 2019. Multiclass speed-density relationship for pedestrian traffic. Transp. Sci. 53 (3), 642–664.
Oeding, D., 1963. Verkehrsbelastung und dimensionierung von gehwegen und anderen anlagen des fußgängerverkehrsstraßenbau und straßenverkehrstechnik, Heft 22, in German.
Older, S., 1968. Movement of pedestrians on footways in shopping streets. Traffic Engineering & Control 10, 160–163.
Peng, J., Wei, Z., Wang, S., Chen, Y., Li, Y., Wang, Z., Taku, F., 2024. A torsional social force model for simulating rotation behavior of pedestrians under multiple scenarios. Transp. Res. Part C Emerging Technol. 163, 104630.
Seyfried, A., Passon, O., Steffen, B., Boltes, M., Rupprecht, T., Klingsch, W., 2009. New insights into pedestrian flow through bottlenecks. Transp. Sci. 43 (3), 395–406.
Shang, X., Jiang, R., Wong, S.C., Gao, Z., Weng, W., 2024. Development and experimental validation of a humanoid pedestrian model that captures stepping behavior and body rotation. Transp. Res. Part C Emerging Technol. 158, 104446.
Shoulson, A., Marshak, N., Kapadia, M., Badler, N.I., 2014. ADAPT: The agent development and prototyping testbed. IEEE Trans. Vis. Comput. Graph. 20 (7), 1035–1047.
Smith, A.J.J., Lemaire, E.D., 2018. Temporal-spatial gait parameter models of very slow walking. Gait Posture 61, 125–129.

Snaterse, M., Ton, R., Kuo, A.D., Donelan, J.M., 2023. Distinct fast and slow processes contribute to the selection of preferred step frequency during human walking. J. Appl. Physiol. 110 (6), 1682–1690.
Song, X., Xie, H., Sun, J., Han, D., Cui, Y., Chen, B., 2019. Simulation of pedestrian rotation dynamics near crowded exits. IEEE Trans. Intell. Transp. Syst. 20 (8), 3142–3155.
Stüvel, S.A., Magnenat-Thalmann, N., Thalmann, D., Van Der Stappen, A.F., Egges, A., 2017. Torso crowds. IEEE Trans. Vis. Comput. Graph. 23 (7), 1823–1837.
von Sivers, I., Köster, G., 2015. Dynamic stride length adaptation according to utility and personal space. Transp. Res. B Methodol. 74, 104–117.
Wageningen-Kessels, F., Daamen, W., Hoogendoorn, S.P., 2018. Two-dimensional approximate Godunov scheme and what it means for continuum pedestrian flow models. Transp. Sci. 52 (3), 547–563.
Xiao, Y., Gao, Z., Qu, Y., Li, X., 2016. A pedestrian flow model considering the impact of local density: Voronoi diagram based heuristics approach. Transp. Res. Part C Emerging Technol. 68, 566–580.
Xu, Q., Chraibi, M., Tordeux, A., Zhang, J., 2019. Generalized collision-free velocity model for pedestrian dynamics. Physica A 535, 122521.
Yamamoto, H., Yanagisawa, D., Feliciani, C., Nishinari, K., 2019. Body-rotation behavior of pedestrians for collision avoidance in passing and cross flow. Transp. Res. B Methodol. 122, 486–510.
Yi, W., Wu, W., Wang, X., Zheng, X., 2023. Modeling the mutual anticipation in human crowds with attention distractions. IEEE Trans. Intell. Transp. Syst. 24 (9), 10108–10117.
Yuan, Z., Jia, H., Zhang, L., Bian, L., 2017. Simulation of pedestrian behavior in the collision-avoidance process considering their moving preferences. Discret. Dyn. Nat. Soc. 2017 (1), 3678268.
Zhai, C., Wu, W., 2020. A new lattice hydrodynamic model for bidirectional pedestrian flow with consideration of pedestrians' honk effect. Int. J. Mod. Phys. C 31, 2050031.
Zhai, C., Wu, W., Xiao, Y., Luo, Q., Zhang, Y., 2022. Modeling bidirectional pedestrian flow with the perceived uncertainty of preceding pedestrian information. Physica A 597, 127205.
Zhang, B., Gao, Y., Han, Y., Liang, S., Chen, Q., Yu, Z., 2022. Walking characteristics and collision avoidance strategy in bidirectional pedestrian flow: a study focused on the influence of social groups. J. Stat. Mech: Theory Exp. 2022 (7), 073405.
Zhang, J., Klingsch, W., Schadschneider, A., Seyfried, A., 2011. Transitions in pedestrian fundamental diagrams of straight corridors and T-junctions. J. Stat. Mech: Theory Exp. 2011 (6), P06004.
Zhang, J., Klingsch, W., Schadschneider, A., Seyfried, A., 2012. Ordering in bidirectional pedestrian flows and its influence on the fundamental diagram. J. Stat. Mech: Theory Exp. 2012 (2), P02002.
Zipf, G.K., 1949. Human behavior and the principle of least effort. Addison-Wesley Press.